Session 3A7
Computational Electromagnetics

A Fast Algorithm for Computing Band Gaps of Three-dimensional Photonic Crystals
C.-C. Chang (Research Center for Applied Mechanics, Academia Sinica, Taiwan); R.-L. Chern (National Taiwan University, Taiwan); C.-C. Chang (Research Center for Applied Mechanics, Academia Sinica, Taiwan); 808

Numerical Simulation of Nonlinear and Parametric Oscillations in a Semiconductor Resonator Structure
G. S. Makeeva (Penza State University, Russia); O. A. Golovanov (Penza Military Institute of Artillery, Russia); M. Pardavi-Horvath (The George Washington University, USA); 809

Study of a Simple Geometry Illuminating Convergence Issues in the Method of Auxiliary Sources
G. Fikioris (National Technical University, Greece); 813

A Parallel Computer Implementation of Fast Low-rank QR Approximation of the Biot-Savart Law
D. A. White (Lawrence Livermore National Laboratory, USA); B. J. Fasenfest (Lawrence Livermore National Laboratory, USA); M. L. Stowell (Lawrence Livermore National Laboratory, USA); 814

Complex Coordinate Transformation as a Radiation Condition in Modal Methods
G. Granet (LASMEA UMR 6602 du CNRS, France); J. P. Plumey (LASMEA UMR 6602 du CNRS, France); K. Edee (LASMEA UMR 6602 du CNRS, France); 819

Full Wave Analysis of RF Signal Attenuation in a Lossy Rough Surface Cave Using a High Order Time Domain Vector Finite Element Method
J. Pingenot (University of Washington,); R. N. Rieben (Lawrence Livermore National Laboratory, USA); D. A. White (Lawrence Livermore National Laboratory, USA); D. G. Dudley (University of Arizona, USA); 820

Direct and Accurate FDTD Modeling of Dispersive Media Using a Fourth-order Rational Conductivity Function
C. Rappaport (Northeastern University, USA); M. Jalalinia (Northeastern University, USA); 825

A Matlab-Based Virtual Propagation Tool: Surface Wave Mixed-path Calculator
L. Sevgi (Doğuş University, Turkey); Ç. Uluışık (Doğuş University, Turkey); 826

Implementation of Arbitrarily Oriented Wires in 3D-TLM Method
B. Larbi (University of Nice-Sophia Antipolis/CNRS, France); J. L. Dubard (University of Nice-Sophia Antipolis/CNRS, France); C. Pichot (University of Nice-Sophia Antipolis/CNRS, France); 833

An Efficient Band Diagonal Preconditioner for Electromagnetic Integral Equations Using Wavelet Packet Bases
A. Geranmayeh (Amirkabir University of Technology, Iran); 834

A Fast Algorithm for Computing Band Gaps of Three-dimensional Photonic Crystals

C.-C. Chang
Research Center for Applied Mechanics, Academia Sinica, Taiwan
R.-L. Chern
National Taiwan University, Taiwan
C.-C. Chang
Research Center for Applied Mechanics, Academia Sinica, Taiwan

In this talk, we present a finite difference formulation for efficiently computing band structures of three-dimensional photonic crystals. First of all, we will show how to correctly discretize the double-curl equation for the magnetic field so that the transversality condition is exactly satisfied in the discrete sense. The first few branches of nontrivial eigenfrequencies that determine the major full band gaps of photonic crystals are computed by interlacing an inverse method with conjugate gradient projection and full multigrid acceleration. The presently developed method is applied to compute band structures of photonic crystals with modified simple cubic lattice, tetragonal square spiral structure (direct and inverse structures), and diamond structure with sp3-like configuration. The computed results for the modified simple cubic and square spiral structures are in close agreement with those obtained by previous authors. Moreover, the sp3-like configuration made of silicon and air is reported to have a large band gap which is larger than the largest reported elsewhere in the literature.

Numerical Simulation of Nonlinear and Parametric Oscillations in a Semiconductor Resonator Structure

G. S. Makeeva[1], O. A. Golovanov[2], and M. Pardavi-Horvath[3]
[1]Penza State University, Russia
[2]Penza Military Institute of Artillery, Russia
[3]The George Washington University, USA

Abstract—The rigorous mathematical modeling of nonlinear oscillations in microwave strip-slot resonator structure (RS), loaded with a distributed planar Gunn diode, is based on the solution of the threedimensional diffraction boundary problem, formulated rigorously taking into account the full set of Maxwell's equations and the nonlinear equation of transport carriers in a semiconductor. Using our numerical approach to determine the bifurcation points of the solution of nonlinear Maxwell's equations, the transition region from the stationary regime of the nonlinear semiconductor device behavior (i. e., the frequency multiplication and the stable parametric amplification) to the generation (the onset of self-oscillations) caused by the instability process in the distributed Gunn diode, was simulated taking into account constrained geometries of strip-slot RS.

1. Introduction

Microwave technology of monolithic integrated/hybrid circuits (MMIC) is moving up to higher frequencies and higher bandwidths, into the mm wave range, up and above 100 GHz. As the industry turns to MMIC devices, planar geometries have to be used. The development and manufacturing of microwave or mm-wave integrated semiconductor devices depends on the development of computer aided design (CAD) tools, based on the accuracy and the adequacy of mathematical models by solving Maxwell's equations rigorously. The goal of the paper is to investigate the nonlinear physical phenomena and effects in a distributed semiconductor insertion, loaded into a resonator structure (RS), using mathematical modeling at the electrodynamic accuracy levels and computing the bifurcation points of the nonlinear Maxwell's operator for the design of prospective MMIC nonlinear semiconductor devices.

2. The Mathematical Model Using the Decompositional Approach on Nonlinear Autonomous Multimode Blocks

The mathematical simulation of nonlinear oscillations in a microwave strip-slot RS, loaded with a distributed planar Gunn diode (Fig. 1) is based on the solution of three-dimensional diffraction boundary value problems for nonlinear Maxwell's equations, complemented with the equation of transport carriers in semiconductor [1]. The computational algorithm for solving the nonlinear diffraction boundary problem is based on the decompositional approach into nonlinear autonomous multimode blocks [2]. The autonomous block, placed between cross-sections S_3 and S_4 (Fig. 1), is nonlinear and it is included in the software package for the mathematical simulation of linear microwave devices [3]. The procedure of the decomposition and recomposition with linear and nonlinear autonomous blocks is described in [2].

For computing of the scattering matrix of the strip-slot resonator and the tapered section in the RS (Fig. 1) a second decomposition was made. The method of the calculation of the scattering matrix of interfaces between regular strip-slot lines (SSL) was proposed in [4], and the method of determining of the scattering matrix of the tapered section is described in details in [5].

The geometry of the tapered section is approximated by a function on $f(z) = \alpha \cdot z - \beta \cdot \sin \gamma \cdot z$, were α, β, γ are approximation coefficients. The accuracy of the results of mathematical modeling of the tapered section depends on the number of step discontinuities p ($p = 10$), the number N of eigenwaves taken into account at the interfaces between regular SSL ($N = 5$) and the number n of the basis functions taken into account at virtual waveguides using the numerical method of multimode autonomous blocks [6] $n = 25$, providing the high accuracy (better than 0.001%) of computation of propagation constants of eigenwaves of SSL.

The mathematical model of the nonlinear semiconductor RS was created by taking into account higher order nonlinearities by using five combination frequencies $M = 5$ [1], the number of eigenwaves on regular SSL for each of the combination frequencies is $N = 5$ at "seaming" of fields at the interfaces between SSL. The mathematical model of the distributed planar Gunn diode accounts for the charging in the semiconductor and the ohmic contacts [1].

3. Accurate Electromagnetic Modeling of Nonlinear and Parametric Effects in the Semiconductor Insertion Loaded into the Resonator Structure

Let a monochromatic electromagnetic wave of frequency ω_1 incident upon the input crosssections S_1, S_2 of RS loaded with the planar Gunn diode (Fig. 1). The waves are the fundamental and the higher-order modes of SSL having known magnitudes $C^+_{n(\alpha)}(\omega_1)$, where α is the index of cross-sections, n are the indexes of eigenwaves of SSL. It is necessary to determine the magnitudes $C^-_{k(\alpha)}(\omega_m)$ of reflected (in local coordinate system on the cross-sections S_1, S_2) modes on combination frequencies ω_m, where m are the indices of the combination frequencies.

The results of computing the normalized magnitudes $\left|C^-_{1(2)}(\omega_2)\right| / \left|C^+_{1(1)}(\omega_1)\right|$ of the reflected (on the output cross-section S_2) fundamental mode at the second time harmonic ($m = 2$), with respect to the magnitude of the incident (on the input cross-sections S_1) fundamental mode at first time harmonic ($m = 1$), depending on the resonator length L for variable magnitudes of $\left|C^+_{1(1)}(\omega_1)\right|$ are represented in Fig. 2. For comparison, the normalized magnitudes $\left|C^-_{1(2)}(\omega_1)\right| / \left|C^+_{1(1)}(\omega_1)\right|$ of the reflected fundamental mode at the first time harmonic ($m = 1$), with respect to the magnitude of the incident fundamental mode, are also shown in Fig. 2.

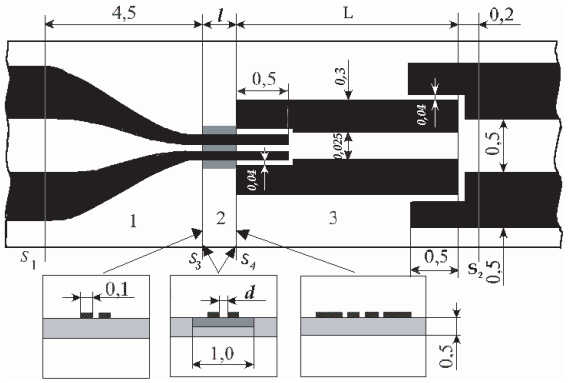

Figure 1: Resonator structure (RS) with the nonlinear semiconductor insert: 1—tapered section; 2—distributed planar Gunn diode; 3—strip-slot resonator (SSR).

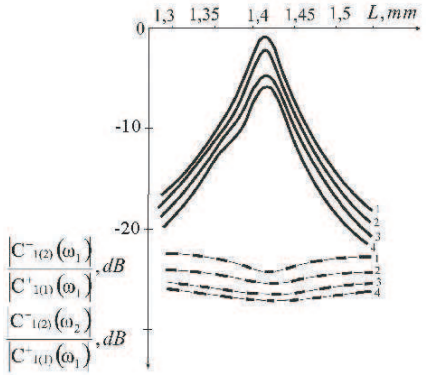

Figure 2: Efficiency of frequency multiplication depending on the resonator length L: curve 1—$C^+_{1(1)}(\omega_1) = 16\,\mathrm{V/mm}$; 2—$24\,\mathrm{V/mm}$; 3—$32\,\mathrm{V/mm}$; 4—$40\,\mathrm{V/mm}$; $f_1 = 30\,\mathrm{GHz}$; $- - -m = 2$, $- - m = 1$

The results of numerical modeling were obtained for the biasing electric field $E_0/\omega_0 = 1000\,\mathrm{V/mm}$ (at point 4 of the observation of electrostatic field [1]), and for the parameters of the epitaxial film $\varepsilon = 12.5$, $\mu = 1$, $D_F = 200\,\mathrm{cm}^2/c$; $n_0 = 1.5 \cdot 10^{15}\,\mathrm{cm}^{-3}$, and the substrate $\varepsilon = 12.5$; $\mu = 1$; the length of planar semiconductor insertion is $l = 0.3\,\mathrm{mm}$.

The results of computing of the normalized magnitudes $\left|C^-_{1(2)}(\omega_2)\right| / \left|C^+_{1(1)}(\omega_1)\right|$, depending on the value of parameter n_0/f, where f is the frequency, n_0 is the electron concentration (in the active layer of the semiconductor $n_0 = N_D$, were N_D is the doping density) for variable $\left|C^+_{1(1)}(\omega_1)\right|$ are represented in Fig. 3(a). For comparison, the normalized magnitudes $\left|C^-_{1(2)}(\omega_1)\right| / \left|C^+_{1(1)}(\omega_1)\right|$ are also shown in Fig. 3(b).

It follows from the results of electromagnetic modeling, shown in Figs. 2 and 3, that the nonlinear effect of frequency multiplication in the distributed planar Gunn diode in the RS depends on changes of magnitudes $C^+_{1(1)}(\omega_1)$ of incident wave. If $C^+_{1(1)}(\omega_1)$ increases, the efficiency of frequency multiplication $K_1(\omega_2) = 20\lg\frac{|C^-_{1(2)}(\omega_2)|}{|C^+_{1(1)}(\omega_1)|}$ decreases (as for the amplification coefficient $K_1(\omega_1) = 20\lg\frac{|C^-_{1(2)}(\omega_1)|}{|C^+_{1(1)}(\omega_1)|}$ at the first time harmonics); because the electromagnetic field is extinguished when the value of the electric field in semiconductor becomes smaller than the Gunn threshold. The nonlinear effect of frequency multiplication is significant for the optimum value of the parameter n_0/f, because charging effects, depending on the ratio of the frequency f and the Gunn effect transit-time frequency, determine the increase of the nonlinearity coefficient of the semiconductor medium even for small values of $C^+_{1(1)}(\omega_1)$.

The results of numerical calculations of parametric amplification coefficient $K_y(\omega_1)$ for small signal case, depending on the distance d between the RS strips, (in fact, d determines the intensity of the biasing electric field

E_0), and taking into account variations of the electron concentration n_0 in the semiconductor, are shown in Fig. 4.

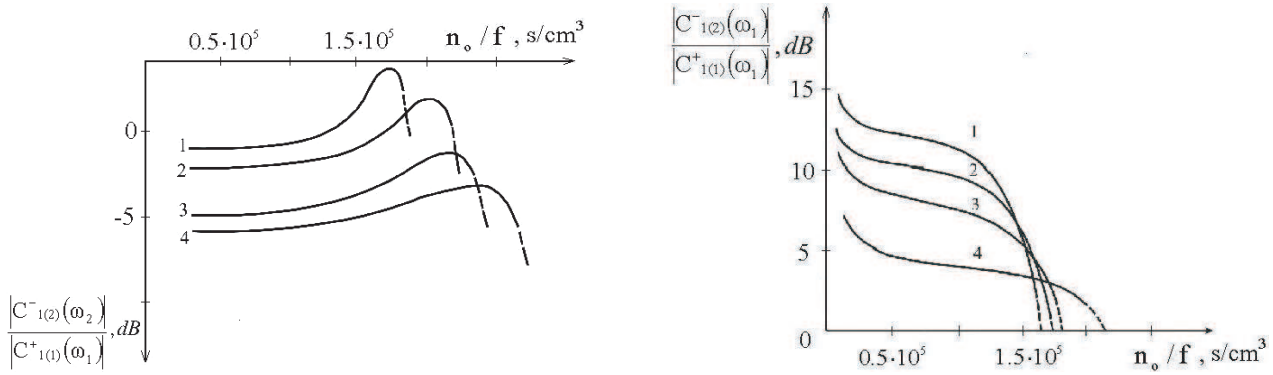

(a) (b)

Figure 3: Efficiency of the frequency multiplication (a) and the amplification coefficient (b) depending on the electron concentration n_0: curve 1– $C^+_{1(1)}(\omega_1) = 16\,\mathrm{V/mm}$; 2– 24 V/mm; 3– 32 V/mm; 4– 40 V/mm; $f_1 = 30\,\mathrm{GHz}$; other parameters are the same as in Fig. 1.

4. Numerical Modeling of the Onset of Self-oscillations by Computing the Bifurcation Points

The numerical method, developed by us in [7], was used to determine the bifurcation points of the nonlinear Maxwell's operator. The generation in the distributed planar Gunn diode loaded into the strip-slot RS, caused by the instability process in the semiconductor with a bulk negative conductivity, was simulated taking into account the constrained geometries. The bifurcation points are those values of the bifurcation parameters, i. e., the frequencies fs, where self-excited oscillations appear [1]. Using the auxiliary computing algorithm [7] the necessary and sufficient conditions for the existence of the bifurcation point [8] in neighborhood of the numerical parameter F can be investigated. If only the sufficient condition, that the eigenvalue of matrix A(z) is an integer [8], is satisfied, in this point the magnitude of self-oscillations is equal to zero for F (see Table 1). If the necessary and sufficient conditions for the existence of the bifurcation point [8] are satisfied, then there is a new solution at the bifurcation point, described by the onset of non-zero magnitude self-oscillations at the bifurcation parameter fs (see Table 1).

Table 1: The bifurcation parameter fs and parameter F depending on the distance d between RS strips, determining the biasing electric field $E_0(\omega_0)$, and the electron concentration n_0.

d, mm	$n_0 = 1.5 \cdot 10^{15}, \mathrm{cm}^{-3}$		$n_0 = 3.5 \cdot 10^{15}, \mathrm{cm}^{-3}$			$n_0 = 5.5 \cdot 10^{15}, \mathrm{cm}^{-3}$		
	F, GHz	$C^-_{1(1,2)}(\omega)$ V/mm	F, GHz	fs, GHz	$C^-_{1(1,2)}(\omega)$ V/mm	F, GHz	fs, GHz	$C^-_{1(1,2)}(\omega)$ V/mm
0.00150	68.90	0.00	68.83		0.00	68.76		0.00
0.00200	51.68	0.00	51.63		0.00		51.58	75.39
0.00250	40.84	0.00		40.80	50.37		40.78	277.31
0.00300	33.98	0.00		33.95	79.56		33.91	398.16
0.00343	30.06	0.00		30.03	170.18		30.00	475.24
0.00400	25.81	0.00		25.78	281.31		25.76	495.23
0.00450	22.71	0.00		22.69	398.28		22.66	470.31
0.00500	20.43	0.00		20.41	451.71		20.39	463.31
0.00550	18.69	0.00		18.67	485.75		18.65	451.57

The results of computing the bifurcation points depending on the value of the intensity of biasing electric field $E_0(\omega_0)$, are determined by the distance d between RS strips, and the electron concentration n_0 in the semiconductor are presented in Table 1, where F is a numerical parameter, fs are the bifurcation parameters, i. e., the frequencies of the onset of self-oscillations, d is the distance between RS strips, n_0 is the electron concentration in the semiconductor, $C^-_{1(1,2)}(\omega)$ are the magnitudes of self-excited oscillations on the output cross-sections S_1, S_2.

The optimum parameters and the size of the planar Gunn diode for the efficiency of the generation and parametric amplification were determined by taking into account constrained geometries. The optimum value of $d = 0.00343\,\text{mm}$ determines the maximum of parametric amplification coefficient $K_y(\omega_1)$ (Fig. 4), when the frequency of self-excited oscillations in the transit-time mode of the planar Gunn diode ($fs = 30\,\text{GHz}$ from Table 1) is equal to the frequency of pumping wave $f = 2f_1$ in the degenerate regime of parametric amplification. At this frequency for $n_0 = 5.5 \cdot 10^{15}\,\text{cm}^{-3}$ the magnitude of self-excited oscillations ($C^-_{1(1,2)}(\omega) = 475.24\,\text{V/mm}$) is more than for $n_0 = 3.5 \cdot 10^{15}\text{cm}^{-3}$ ($C^-_{1(1,2)}(\omega) = 170.18\,\text{V/mm}$), that is why increasing the nonlinearity of the "dynamic capacity" of the planar Gunn diode provides an increasing parametric amplification coefficient $K_y(\omega_1)$ (Fig. 4). It follows from the results of computing (Table 1) that for $n_0 = 1.5 \cdot 10^{15}\,\text{cm}^{-3}$ there is no self-oscillations in the planar Gunn diode, as this is the stable regime of the steady state domains [9].

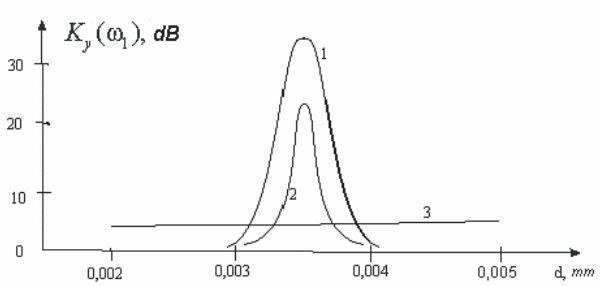

Figure 4: Efficiency of parametric amplification, depending on the distance d between RS strips (i. e., the biasing electric field $E_0(\omega_0)$) for different electron concentrations n_0: 1—$n_0 = 5.5 \cdot 10^{15}\,\text{cm}^{-3}$; 2—$3.5 \cdot 10^{15}\,\text{cm}^{-3}$; 3—$1.5 \cdot 10^{15}\,\text{cm}^{-3}$; $f_1 = 15\,\text{GHz}$, $C^+_{1(1)}(\omega_1)$=0.01 V/mm.

5. Conclusion

The accurate electromagnetic modeling of nonlinear and parametric oscillations in microwave stripslot RS loaded with a distributed planar Gunn diode shows how the efficiency of the frequency multiplication and the parametric amplification depends on the magnitude and the electron concentration in the semiconductor. The results of computing the bifurcation points by our numerical method permit to analyze the optimum parameters and the size of the distributed planar Gunn diode in RS for the efficient generation and parametric amplification taking into account constrained geometries. The new results of research into nonlinear interactions (self-oscillations, frequency multiplication, parametric amplification) in distributed planar semiconductor Gunn diodes could be used for future MMIC devices, in particular, new microwave mm- or submm-wave generators, frequency multipliers, parametric amplifiers.

REFERENCES

1. Makeeva, G. S., O. A. Golovanov, and M. Pardavi-Horvath, "Rigorous nonlinear analysis of propagating waves in the strip-slot waveguiding structure with a strongly nonlinear semiconductor discontinuity," *Progress in Electromagnetics Research Symposium, PIERS 2005*, Hangzhou, China, 22–26, Aug. 2005.
2. Golovanov, O. A., "Nonlinear autonomous blocks and their usage for studying irregular waveguides and resonators with nonlinear media," *Radiofizika*, Izvestiya vysshikh uchebnykh zavedenii, Vol. 33, 793, 1990.
3. Golovanov, O. A., "Computer-aided engineering system for modeling of microwave devices," *Radioelektronika*, Izvestiya vysshikh uchebnykh zavedenii, Vol. 29, 74, 1986.
4. Nikolskiy, V. V., V. V. Orlov, and V. P. Feoktistov, "Computer aided design (CAD)of microwave devices," *M. Radio and Sviaz*, 272, 1982.
5. Golovanov, O. A., "Research of tapered section between planar lines and rectangular waveguides," *Radiotekhnika i Elektronika*, Vol. 32, 182, 1987.
6. Nikolskiy, V. V. and O. A. Golovanov., "Autonomous multimode blocks and their application to the analysis of a strip line," *Radiotekhnika i Elektronika*, Vol. 24, 1070, 1979.
7. Makeeva, G. S., O. A. Golovanov, and M. Pardavi-Horvath, "Numerical analysis of wave instability in strongly nonlinear ferrite structures using bifurcation points of the nonlinear Maxwell's operator," *Progress in Electromagnetics Research Symposium, PIERS 2005*, N041209144900, Hangzhou, China, 22–26, Aug. 2005.
8. Krasnoselskiy, M. A., *Functional Analysis*, Nauka, Moscow, 1964.
9. Makeeva, G. S., O. A. Golovanov, and V. E. Lybchenko, "The bifurcation analysis of nonlinear oscillations in resonator structures with distributed semiconductor insertions," *Seriya Nature Science*, Izvestiya vysshikh uchebnykh zavedenii, Povoljskyi Region, Vol. 6, 137, 2003.

Study of a Simple Geometry Illuminating Convergence Issues in the Method of Auxiliary Sources

G. Fikioris
National Technical University, Greece

The Method of Auxiliary Sources (MAS) is often applied to problems involving a closed, smooth, perfect conductor (PEC), illuminated by an external source: One seeks to approximately satisfy the boundary conditions on the PEC surface using a large number of fictitious sources located inside the surface. Once these sources are determined, one can calculate quantities such as the PEC surface current, or the (total) field. It is natural to understand MAS "convergence" as convergence of the field thus determined to the true field as the number of fictitious sources increases indefinitely. It is known that convergence has to do with the singularities of the true field when extended to the region inside the PEC surface.

Recent papers (e.g., [1, 2]) apply MAS to the case where the aforementioned scatterer is an infinitely long circular cylinder. For this simple special geometry, for which much can be done analytically, the results helps one understand various aspects of MAS and can be used to investigate the accuracy of MAS.

The present paper revisits the infinitely long circular cylinder, but focuses on the issue of convergence. For certain external illuminations and auxiliary-source configurations, we show that an alternative (to the above) concept of "convergence" — namely, convergence of the MAS sources themselves — can also be useful. Although convergence is often unambiguous, there exist cases where the scattered field converges while the MAS sources diverge. Using simple manipulations, we develop conditions — related to the aforementioned singularities of the true field — for this phenomenon to occur. We show that our detailed analytical results (which are possible because of the simplicity of our geometry) provide insight into MAS in general. We point out many similarities between our results and recent studies on the application of numerical methods to Hallen's and Pocklington's equations with the approximate kernel [3].

REFERENCES

1. Larsen, N. V. and O. Breinbjerg, *J. of Electromagn. Waves and Appl.*, Vol. 18, 745–761, 2004.
2. Anastassiu, H. T., D. G. Lymperopoulos, and D. I. Kaklamani, *IEEE Trans. Antennas Propagat.*, Vol. 52, 1541–1547, 2004.
3. Fikioris, G. and T. T. Wu, *IEEE Trans. Antennas Propagat.*, Vo. 49, 383–392, 2001.

A Parallel Computer Implementation of Fast Low-rank QR Approximation of the Biot-Savart Law

D. A. White, B. J. Fasenfest, and M. L. Stowell
Lawrence Livermore National Laboratory, USA

Abstract—In this paper we present a low-rank QR method for evaluating the discrete Biot-Savart law on parallel computers. It is assumed that the known current density and the unknown magnetic field are both expressed in a finite element expansion, and we wish to compute the degrees-of-freedom (DOF) in the basis function expansion of the magnetic field. The matrix that maps the current DOF to the field DOF is full, but if the spatial domain is properly partitioned the matrix can be written as a block matrix, with blocks representing distant interactions being low rank and having a compressed QR representation. The matrix partitioning is determined by the number of processors, the rank of each block (i. e., the compression) is determined by the specific geometry and is computed dynamically. In this paper we provide the algorithmic details and present computational results for large-scale computations.

1. Introduction

The computation of magnetic fields from a prescribed electric current is a common problem in magnetic design and analysis. One approach is to form the problem as a Partial Differential Equation (PDE) for the unknown field with the prescribed electric current as the source term. Regardless of the particular PDE formulation, e. g., a magnetic vector potential formulation or a mixed B-H formulation, a large volumetric mesh must be employed, and some boundary condition must be applied on the outer boundary of the mesh. In contrast to the PDE approach, the Biot-Savart law can be employed to directly compute the magnetic field due to the prescribed current [1]. The advantage of the Biot-Savart law approach is that a full volume mesh is not required, and no boundary conditions need be applied. The disadvantage of the Biot-Savart approach is the computational cost, if there are $O(N)$ magnetic field observation points and $O(M)$ current samples the cost is $O(N * M)$. In this paper we review a fast low-rank QR method for compressing the $M \times N$ Biot-Savart matrix. The approach is similar to low-rank QR methods developed for boundary element electrostatics [2, 3] and for low frequency electric field integral equations [4]. The key difference with our approach is that we are concerned with volumetric current densities and implementation on parallel computers.

2. Formulation

The law of Biot and Savart is given by

$$\vec{B}(x) = \nabla \times \vec{A} = \frac{1}{\mu 4\pi} \int_{\Omega'} \frac{\vec{J}(x') \times (x - x')}{|x - x'|^3} d^3x'. \tag{1}$$

where $J(x')$ is the known current density at the source point x', and $B(x)$ is the desired magnetic flux density at the observation point x. We assume that we have a finite element representation for J over the volume Ω', and a finite element representation for B over a surface Γ,

$$\vec{J} = \sum_{i=1}^{N} \xi_i \vec{W}_i^2, \quad \vec{B} = \sum_{j=1}^{M} \beta_j \vec{W}_j^1, \tag{2}$$

where ξ_j and β_j are the ith degree-of-freedom (DOF), and $\vec{W}_i^2$ and $\vec{W}_j^1$ are vector basis functions. Inserting the basis function expansions (2) into (1) yields the discrete Biot-Savart law

$$\mathbf{M}\bar{\beta} = \mathbf{Z}\bar{\xi}, \tag{3}$$

where

$$\mathbf{Z}_{ij} = \int_{\Gamma} \int_{\Omega'} \frac{1}{\mu 4\pi} \frac{\vec{W}_i^2(x') \times (x - x') \cdot \vec{W}_j^1(x)}{|x - x'|^3} d\Omega' d\Gamma, \tag{4}$$

and

$$\mathbf{M}_{ij} = \int_{\Gamma} \vec{W}_i^1(x) \cdot \vec{W}_j^1(x) d\Gamma \tag{5}$$

and where $\bar{\xi}$ and $\bar{\beta}$ are the arrays of DOF. The matrix $\mathbf{M}$ is a "mass matrix" due to the fact that the basis functions are not orthogonal. The mass matrix is extremely sparse and the computational cost for forming and solving this matrix is negligible. In many applications the problem of determining the B-field can be posed in terms of the magnetic vector potential $A = \nabla \times B$ with

$$\vec{A}(x) = \frac{1}{\mu 4\pi} \int_{\Omega} \frac{\vec{J}(x')}{|x - x'|} d^3x'. \tag{6}$$

Using a finite element representation for A yields another version of the discrete Biot-Savart law

$$\vec{J} = \sum_{i=1}^{N} \xi_i \vec{W}_i^2, \quad \vec{A} = \sum_{j=1}^{M} \alpha_j \vec{W}_j^1, \tag{7}$$

$$\mathbf{M}\bar{\alpha} = \mathbf{Y}\bar{\xi}, \tag{8}$$

where

$$\mathbf{Y}_{ij} = \int_{\Gamma} \int_{\Omega'} \frac{1}{\mu 4\pi} \frac{\vec{W}_i^2(x') \cdot \vec{W}_j^1(x)}{|x - x'|} d\Omega' d\Gamma. \tag{9}$$

We will refer to the $M \times N$ matrices $\mathbf{Z}$ and $\mathbf{Y}$ as Biot-Savart matrices. The computation of these matrices involves singular and near-singular integrals. The surface integration is performed using standard Gaussian quadrature points for each surface element. The volume integration uses an adaptive integration rule, which varies the order of Gaussian quadrature based on the distance between the source point x' and the observation point x. When the surface element containing x is a face of the volume element containing x', a highly accurate height-based singularity cancellation quadrature rule is used [5]. The matrices (4) and (9) are constructed using 2-form or "face elements" for the basis functions W^2 and 1-form or "edge elements" for the basis functions W^1, see [6] for details on the construction of the basis functions.

Our primary application for the discrete Biot-Savart law is providing boundary conditions for finite element solution of multi-conductor eddy current problems. In each conductor we solve the time-dependent vector diffusion equation using an edge element based A-ϕ finite element formulation [7]. Clearly the B-field in the air surrounding the conductors is critical. The finite element formulation requires that either $\hat{n} \times \vec{A}$ or $\hat{n} \times \vec{B}$ be specified on the conductor boundaries, corresponding to inhomogeneous Dirichlet or Neumann boundary conditions, respectively. Our approach for dealing with the B-field in the air surrounding the conductors is to use the discrete Biot-Savart law (3) or (8) as the boundary condition on each conducting surface.

3. Parallel Implementation

We assume that the volume Ω has been partitioned into K partitions, where K is the number of computational processors, with each partition having an equal number of volume elements. The volume elements are distributed via the partitioning. The surface Γ is also partitioned into K equally sized surface partitions. Note however that the surface elements are not distributed via the surface partitions, each processor can access the entire surface mesh. The Biot-Savart matrix is then decomposed into a $K \times K$ block matrix, with every block $Z^{pq}, p \in \{1:K\}, q \in \{1:K\}$ representing the interaction of surface partition Γ_p with volume Ω_q. The qth processor computes blocks $Z^{pq}, p = 1:K$, i. e., a column of blocks. Note that the matrix is decomposed via a partitioning of elements, hence the matrices Z^{pq} are overlapping in DOF space. The specific partitioning algorithm used to partition the elements is not critical, in the examples below we employ a graph-based algorithm [8]. The key point is that if the partitions Γ_p and Ω_q are well-separated then the sub-matrix Z^{pq} will have a low-rank QR decomposition. The procedure for computing the low-rank QR decomposition is described below. We define "well-separated" as follows: the bounding spheres for the element partitions Γ_p and Ω_q are computed, if the bounding spheres do not intersect then the partitions are considered well-separated and a low-rank QR representation of Z^{pq} is computed. We employ a recursive procedure for computing Z^{pq} when partitions Γ_p and Ω_q are not well-separated. This results in a hierarchical representation for Z. If Γ_p and Ω_q are not well separated, Ω_q is divided into eight equally sized sub-partitions, Γ_p is divided into four equally sized sub-partitions, and the "well-separated test" is applied to the sub-partitions Γ_{pi} and Ω_{qj}, $i = 1:4$, $j = 1:8$. A

space-filling curve algorithm is used for creating the sub-partitions. The process is applied recursively, with a low-rank QR representation computed for well-separated sub-partitions. The recursion is halted when a volume sub-partition contains fewer than some number of elements, for application example 512. If at the lowest level of recursion the interaction is not well separated, it is simply represented by a dense matrix.

No parallel communication is required in the construction of the hierarchical Biot-Savart matrix, each processor has the elements that it needs to perform the integrals. Each processor has the same amount of work hence the computation of is load balanced. Note, however, that in the low-rank QR approximation the rank k is computed dynamically, and the rank k depends upon the geometry. Hence the application of the hierarchical Biot-Savart matrix, i. e., the matrix-vector multiplication $\bar{\beta} = \mathbf{Z}\bar{\xi}$, may not be perfectly load balanced. Also note that the application of the hierarchical Biot-Savart matrix does require parallel communication. This communication is as follows: (1) each processor q does a gather operation to get the values of $\bar{\xi}$ that it needs, (2) each processor q loops over the sub-matrices Z^{pq}, $p = 1 : K$ and computes $\bar{\beta}_q = \mathbf{Z}^{pq}\bar{\xi}_q$, (3) each processor participates in a global reduction on $\bar{\beta}_q$.

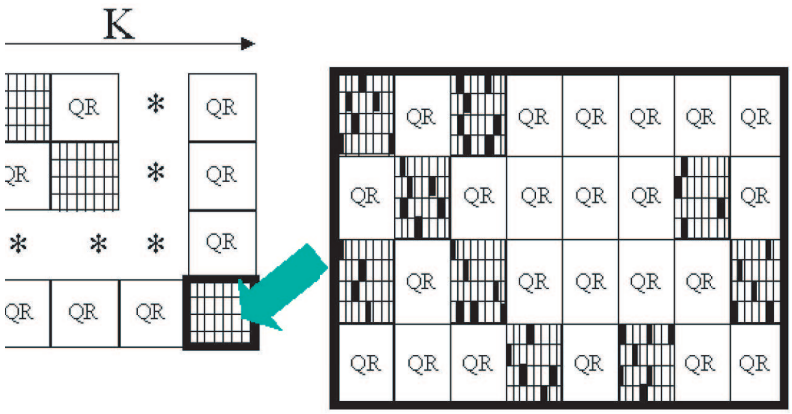

Figure 1: Hierarchical partitioning of the Biot-Savart matrix. The highest level of partitioning is based on the number of processors, as represented by the left-most matrix. The sub-matrices Z^{pq} representing near interactions are hierarchically decomposed into 8 sub-volumes and 4 sub-surfaces, as illustrated by the rightmost matrix.

4. Low-rank QR Decomposition

When Γ_p and Ω_q are well separated the matrix Z^{pq} will have a low-rank representation

$$Z^{pq}_{m\times n} \approx Q_{m\times k} \times R_{k\times n}, \tag{10}$$

where k is the rank. We do not want to form the entire Z^{pq} and then compress it, rather we sample the matrix by picking s rows and columns of Z^{pq}, where s is some predetermined number, e. g., 50. The procedure for picking the sampled rows and columns is ad-hoc, the procedure that we employ is described in [4]. The sampling procedure is solely linear algebra, it does not depend upon the particular Green's function, finite element basis functions, etc. For the ad-hoc sampling procedure to be effective we must have s greater than the expected rank. The algorithm for computing $Q_{m\times k}$ and $R_{k\times n}$ is as follows:

Step 1: Form the sampled column matrix $S^c_{m\times s}$ and the sampled row matrix $S^r_{s\times n}$.

Step 2: Compute the rank-revealing QR decomposition $\tilde{Q}_{m\times s}\tilde{R}_{s\times s} = S^c_{m\times s}$ using LAPACK routines DGEQPF and DORGQR. The rank k is determined by the criteria $\tilde{R}_{kk} < thresh \cdot \tilde{R}_{11}$ where $thresh$ is a threshold value, we then keep only k columns of $\tilde{Q}$, denote this as $Q_{m\times k}$, and discard $\tilde{R}$.

Step 3: We form a new matrix $\hat{Q}_{s\times k}$ by taking s rows of $Q_{m\times k}$, the exact same rows as used to construct S^r.

Step 4: Compute the least-squares solution to $\hat{Q}_{s\times k}R_{k\times n} = S^r_{s\times n}$ using LAPACK routine DGELSS.

At this point we have the desired matrices $Q_{m\times k}$ and $R_{k\times n}$ which approximate $Z^{pq}_{m\times n}$. The quality of the approximation, and the amount of compression (the rank k), are determined by the value of $thresh$ used in Step 2 above. Our approach, being based on highly tuned LAPACK routines, is efficient both in terms of FLOPS

and memory usage. The complexity is $O(m \cdot s) + O(s \cdot n)$, using a fixed value of s yields a linear complexity in m and n.

5. Examples

In these examples we compute a hierarchical low-rank QR approximation of the matrix defined by Eq.(9). For the first example consider the geometry shown in Fig. 2. This geometry consists of 19000 volume elements and is partitioned for 16 processors. Therefore the Biot-Savart matrix will be a 16×16 block matrix. Each block Z^{pq} has roughly 1200 rows and 4000 columns. Using values of $s = 50$ and $thresh = 0.005$ gives the parallel rank map shown in (11). The compression is significant, each 1200×4000 matrix is compressed to $Q_{1200 \times k} + R_{k \times 4000}$ where k is the value shown in (11). Note that the blocks labeled with rank 00 are near interactions and have full rank. These blocks were decomposed further as explained in Section 3 above. For example, the Z^{11} near-interaction matrix will be decomposed into 8 sub-volumes and 4 sub-surfaces, each resulting sub-matrix has roughly 270 rows and 560 columns. The resulting rank map for the Z^{11} sun-matrix is shown in (12). Again the blocks labeled with rank 00 are near-interactions and have full rank. In this specific case the sub-partitions have around 150 volume elements each, so they will not be partitioned further. The total compression was $60\times$ for this specific example.

The second example is shown in Fig. 3. The geometry consists of three conducting coils, the center coil is driven with an independent current source, and we wish to compute the eddy currents in the coils due to the B-field in the surrounding air. The problem consists of 20736 volume elements and was partitioned for 24 parallel processors, therefore the Biot-Savart matrix is a 24×24 block matrix. The parallel rank map for this is too large to show here, but the results were as follow: Each processor had 24 matrices to compute at the highest level, on average 19 of these corresponded to well-separated regions and were compressed with an average rank of 10. The remaining 5 full-rank matrices were further partitioned into $4 \cdot 8 = 32$ sub-matrices, and on average 29 of these corresponded to well-separated regions and were compressed with an average rank of 25. At the lowest level of the hierarchy, the near interactions were represented, on average, by dense matrices of dimension 335×439, there were a total of $24 \cdot 3 = 72$ of these. The total compression was $109\times$. This compression represents both the memory savings and the reduction in CPU time required to apply the Biot-Savart interaction.

$$\begin{bmatrix}
00 & 14 & 16 & 00 & 12 & 10 & 5 & 8 & 5 & 4 & 12 & 20 & 12 & 7 & 7 & 7 \\
5 & 6 & 6 & 5 & 8 & 12 & 00 & 21 & 00 & 21 & 6 & 4 & 9 & 11 & 18 & 11 \\
19 & 00 & 21 & 00 & 00 & 17 & 7 & 12 & 11 & 7 & 00 & 12 & 24 & 12 & 10 & 10 \\
11 & 00 & 12 & 12 & 00 & 00 & 11 & 00 & 15 & 9 & 17 & 7 & 13 & 14 & 12 & 19 \\
6 & 13 & 11 & 9 & 16 & 00 & 14 & 00 & 00 & 12 & 6 & 12 & 16 & 14 & 23 & 5 \\
6 & 6 & 5 & 8 & 12 & 00 & 21 & 00 & 21 & 6 & 4 & 9 & 11 & 18 & 11 & 5 \\
9 & 7 & 7 & 10 & 34 & 00 & 00 & 00 & 15 & 8 & 5 & 9 & 12 & 18 & 17 & 21 \\
12 & 00 & 16 & 9 & 9 & 4 & 8 & 5 & 4 & 12 & 00 & 15 & 9 & 6 & 8 & 19 \\
16 & 00 & 17 & 17 & 11 & 5 & 9 & 6 & 6 & 45 & 00 & 44 & 12 & 8 & 10 & 13 \\
00 & 12 & 14 & 00 & 00 & 9 & 23 & 12 & 8 & 25 & 9 & 16 & 11 & 11 & 13 & 11 \\
21 & 21 & 12 & 24 & 11 & 8 & 12 & 12 & 9 & 00 & 12 & 00 & 00 & 12 & 29 & 10 \\
14 & 12 & 10 & 16 & 19 & 9 & 17 & 12 & 10 & 00 & 9 & 00 & 00 & 15 & 00 & 5 \\
8 & 5 & 7 & 7 & 11 & 20 & 12 & 15 & 00 & 6 & 5 & 8 & 12 & 00 & 18 & 6 \\
9 & 11 & 8 & 10 & 18 & 9 & 22 & 14 & 16 & 13 & 6 & 12 & 00 & 45 & 00 & 5 \\
8 & 7 & 6 & 10 & 11 & 15 & 20 & 16 & 00 & 9 & 4 & 11 & 37 & 00 & 00 & 15 \\
38 & 00 & 16 & 00 & 16 & 11 & 7 & 11 & 10 & 7 & 00 & 15 & 00 & 14 & 12 & 11
\end{bmatrix} \tag{11}$$

$$\begin{bmatrix}
00 & 11 & 19 & 38 & 00 & 12 & 31 & 21 \\
23 & 16 & 21 & 16 & 00 & 36 & 17 & 27 \\
26 & 00 & 35 & 00 & 14 & 23 & 43 & 33 \\
26 & 13 & 00 & 42 & 41 & 13 & 00 & 00
\end{bmatrix} \tag{12}$$

The difference in compression for these two examples, 60x vs 109x, indicates that the amount of compression depends upon the number of elements, greater compression will be a achieved as the computational mesh is refined. If the computational mesh were refined, the well-separated interactions would still have the same rank, hence the cost of the well-separated interactions is $O(N)$. Each near-interaction is recursively decomposed into $4 \cdot 8 = 32$ interactions, most of which are again well-separated and have low-rank. The dominant cost

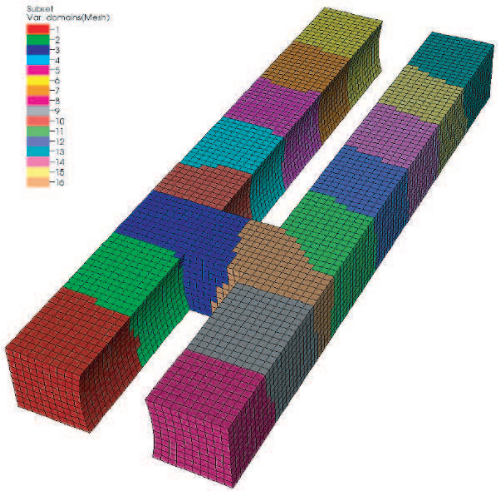

Figure 2: Computational mesh for a linear induction motor partitioned for 16 parallel processors.

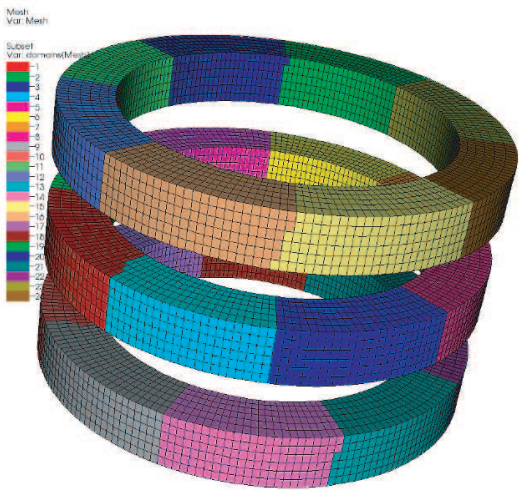

Figure 3: Computational mesh for an inductive coupling application partitioned for 24 parallel processors.

is the nearinteractions which are represented as dense $m \times n$ matrices, where m and n are determined by fixed parameters (e. g., the recursion halting parameter of 512 elements) which are independent of the global dimensions M and N. The number of near interactions is, asymptotically, $O(N\,log(N))$, hence the overall method is $O(N\,log(N))$.

Acknowledgement

This work was performed under the auspices of the U.S. Department of Energy by the University of California, Lawrence Livermore National Laboratory under contract No. W-7405-Eng-48.

REFERENCES

1. Jackson, J. D., *Classical Electrodynamics*, 1962.
2. Kapur, S. and D. Long, "IES3: Efficient electrostatic and electromagnetic solution," *IEEE Comp. Sci. Eng.*, Vol. 5, No. 4, 60–67, 1998.
3. Gope, D. and V. Jandhyala, "PILOT: A fast algorithm for enhanced 3d parasitic capacitance extraction," *Micro. Opt, tech. Lett.*, Vol. 41, No. 3, 169–173, 2004.
4. Gope, D. and V. Jandhyala, "Efficient solution of EFIE via low-rank compression of multilevel predetermined interactions," *IEEE Trans. Ant. Prop.*, Vol. 53, No. 10, 3324–3333, 2005.
5. Khaya, M. A. and D. R. Wilton, "Numerical evaluation of singular and near-signular potential integrals," *IEEE Trans. Ant. Prop.*, Vol. 53, No. 10, 3180–3190, 2005.
6. Castillo, P., J. Koning, R. Rieben, and D. White, "A discrete differential forms framework for computational electromagnetics," *Computer Modeling in Engineering & Sciences*, Vol. 5, No. 4, 331–346, 2004.
7. Rieben, R. and D. White, "Verification of high-order mixed FEM solution of transient magnetic diffusion problems," *IEEE Trans. Mag.*, October 2005. article in press.
8. Karypis, G. and V. Kumar, "A parallel algorithm for multilevel graph partitioning and sparse matrix ordering," *J. Parallel Distr. Comp.*, Vol. 48, No. 1, 71–95, 1998.

Complex Coordinate Transformation as a Radiation Condition in Modal Methods

G. Granet, **J. P. Plumey**, **and K. Edee**
LASMEA UMR 6602 du CNRS, France

Modal methods and mode matching techniques are well established methods to solve wave guide and scattering problems. Such methods lead to an eigenvalue problem that is transformed into a numerical matrix eigenvalue problem by the method of moments. At this step, the boundary conditions that the field of the physical problem have to satisfy are included in the chosen expansion basis. For instance we chose periodic functions with a pseudo periodic coefficient to represent the field in grating problems or sine function to represent a field that should be zero on some boundary.

When considering problems in which radiation occurs (for instance leaky waves or discontinuities) we face a dilemma: on one hand we would wish to obtain the correct solution and properly takes into account the radiation boundary condition, on the other hand we would like to go on using the numerical tools that we have already developed and optimised. Some ten years ago, those who were using the finite difference time domain method faced also a similar problem. An elegant and efficient solution was then proposed by Berenger [1] who has introduced the concept of the so called perfect matched layers (PML).

Derudder et al. [2] showed that PML could also be very useful in modal methods. Since the pioneer work of Berenger many alternatives have been developed, one of which is the co-ordinate stretching introduced by Chew et al. [3]. We also adopt this point of view that can be easily combined with our own parametric approach [4]. We thus obtain efficient numerical tools able to analyse most guided wave problems including those with surface waves like plasmons. Furthermore, the conjunction of periodic functions and stretched co-ordinates also allows to derive a fast converging series expansion for the Green's function of layered media.

In this presentation, we shall describe from the operator point of view the implementation of the stretched co-ordinates as a radiation condition in any co-ordinate system. We will also discuss the accuracy limits of the proposed approach as a function of the various stretching parameters. Many examples will be given including radiation by structures that support plasmons and radiation by sources embedded in layered media with corrugated interfaces.

REFERENCES

1. Berenger, J. P., "A perfectly matched layer for the absorption of electromagnetic waves," *J. Comput. Phys.*, Vol. 114, 185–200, 1994.
2. Derudder, H., F. Olyslager, and D. De Zutter, "An efficient series expansion for the 2-D Green's function of a microstrip substrate using perfectly matched layers," *IEEE Microwave Guided Wave Lett.*, Vol. 9, No. 12, 505–507, 1999.
3. Chew, W. C. and W. H. Weedon, "A 3-D perfectly matched medium from modified Maxwel's equations with stretched coordinates," *Microwave Opt. Technol. Lett.*, Vol. 7, No. 13, 599–604, 1994.
4. Granet, G., "Reformulation of the lamellar grating problem through the concept of adaptive spatial resolution," *Journal of Optical Society of America A*, Vol. 16, No. 10, 2510–2516, 1999.

Full Wave Analysis of RF Signal Attenuation in a Lossy Rough Surface Cave Using a High Order Time Domain Vector Finite Element Method

J. Pingenot
University of Washington, USA

R. N. Rieben and D. A. White
Lawrence Livermore National Laboratory, USA

D. G. Dudley
University of Arizona, USA

Abstract—We present a computational study of signal propagation and attenuation of a 200 MHz planar loop antenna in a cave environment. The cave is modeled as a cylindrical guiding structure with a lossy wall. The wall is nominally circular with a random roughness. To simulate a broad frequency band, the full wave Maxwell equations are solved directly in the time domain via a high order vector finite element discretization using the massively parallel CEM code EMSolve. The numerical technique is first verified against theoretical results for a planar loop antenna in a smooth lossy cave. The simulation is then performed for a series of random rough surface meshes in order to generate statistical data for the propagation and attenuation properties of the antenna in a cave environment. Results for the mean and variance of the power spectral density of the electric field are presented and discussed.

1. Introduction

The study of electromagnetic wave propagation in caves and tunnels is of great practical interest to antenna engineers due to the increasing demands for reliable wireless communications systems in such environments. Current wireless radio frequency (RF) communication systems were not designed to operate reliably in enclosed environments such as caves and tunnels, and signal quality is severely compromised due to the rough and lossy surfaces of the cave. Today there is limited ability to maintain communications in cave-like structures, tunnels or subways, prohibiting the quick deployment of wireless systems in caves and tunnels. If the propagation properties of the tunnel could be better characterized (dissipation, dispersion, fading, and channel capacity), then a more robust communication system could be designed specifically for operation in such environments, hence full wave EM simulations of propagation in this type of environment are very useful.

Much theoretical work in this field has been done in order to develop a better understanding of the RF propagation channel. Dudley recently studied models for propagation in lossy circular tunnels [1]. He produced expressions for the fields in terms of a Fourier transform over the axial variables, and presented the numerical results for the field intensity both as a function of axial distance and as a function of radial distance. However, this work only involved smooth tunnel walls and not the more realistic situation of rough wall tunnels. In this case, the electromagnetic fields can be modeled as a stochastic process in a cave with random rough walls. Recently, Pao and Casey have investigated the statistical properties of wave propagation in straight, rough-walled tunnels [2, 3]. This work assumes a perfect electrical conductor (PEC) boundary at the rough wall/air interface. A more realistic model needs to take into account the lossy nature of the rough walls and the cave material (typically granite or some sort of earth like material with electrical conductivities on the order of 0.1 S/m).

In this paper we use a high order finite element discretization to solve the full wave Maxwell equations directly in the time domain for the case of a planar loop antenna placed at the mouth of a straight, lossy rough walled tunnel. We chose a time domain simulation in order to efficiently compute the response over a broad frequency band. We begin with a brief description of the numerical method employed for this problem (as implemented in the EMSolve code [4]). We then verify the numerical method against the theoretical results of Dudley [1] for a planar loop antenna in a smooth lossy cave and discuss the limitations of the numerical model. Finally, we proceed to solve the electromagnetic wave equation on a sequence of randomly generated meshes to determine statistical properties for the power spectral density of the electric field.

2. Numerical Formulation

We begin with the second order time dependent wave equation for the electric field in a 3 dimensional domain Ω

$$\begin{aligned} \epsilon \frac{\partial^2}{\partial t^2}\mathbf{E} &= -\nabla \times (\mu^{-1}\nabla \times \mathbf{E}) - \sigma \frac{\partial}{\partial t}\mathbf{E} - \frac{\partial}{\partial t}\mathbf{J} && \text{in } \Omega \\ \nabla \cdot (\epsilon \mathbf{E}) &= 0 && \text{in } \Omega \\ \hat{\mathbf{n}} \times \mathbf{E} &= \mathbf{E}_{bc} && \text{on } \partial\Omega \end{aligned} \tag{1}$$

where $\partial\Omega$ is the two dimensional boundary of the domain, $\hat{\boldsymbol{n}}$ is the outwardly directed unit normal of this boundary and $\mathbf{J}$ is a free current density source that can be added to drive the problem. The value $\mathbf{E}_{bc}$ represents an arbitrary boundary condition imposed on the electric field intensity while ϵ, μ and σ denote, respectively, the dielectric permittivity, magnetic permeability and electrical conductivity of the materials contained in the domain Ω.

Applying an arbitrary order Galerkin finite element discretization to the wave equation (the details of which can be found in [5, 6]) yields the following semi-discrete system of ordinary differential equations

$$M_\epsilon \frac{\partial^2}{\partial t^2} e = -S_\mu e - M_\sigma \frac{\partial}{\partial t} e - \frac{\partial}{\partial t} j \tag{2}$$

where M_ϵ, M_σ are finite element mass matrices, S_μ is a finite element stiffness matrix and e, j are discrete arrays of finite element degrees of freedom. Applying a backward difference approximation for the first order time derivative in (2) and a central difference approximation for the second order time derivative yields the following fully discrete linear system of equations

$$M_\epsilon e_{n+1} = (2M_\epsilon - \Delta t^2 S_\mu - \Delta t M_\sigma)e_n + (\Delta t M_\sigma - M_\epsilon)e_{n-1} - j' \tag{3}$$

where Δt is the discrete time step, the integer n denotes the current time step and the time derivative of the free current source has been directly incorporated into the new source term *j'*.

For the results shown in section 4 below we employ second-order interpolatory *H(curl)* basis functions along with custom quadrature rules that yield a diagonal "mass" matrix M_ϵ. The details of this discretization are presented in [7]. This method is much more accurate than standard FDTD. Indeed, the numerical dispersion for this method is $O(h^4)$ rather than $O(h^2)$ as it is for FDTD. Compared to higher-order FDTD schemes, this method is better at modeling the jump discontinuity of fields across the air-earth interface.

3. Verification

Before we proceed to simulations of a random rough surface, we begin by verifying our numerical method with known theoretical values for the case of a smooth, lossy tunnel. These results were computed by Dudley according to the procedures described in [1]. We consider the case of an axially symmetric circular current loop of radius $b = 0.2\,\text{m}$ placed at the mouth of a circular tunnel of radius $a = 2.0\,\text{m}$. The current loop is driven by a time harmonic source of frequency $f = 200\,\text{MHz}$. The electric field is "measured" along the length of the tunnel at a radial observation point ρ such that $\rho/a = 0.3$. The tunnel has a relative dielectric constant of $\epsilon_r = 5.0$. We consider two cases, a tunnel with an electric conductivity $\sigma_{low} = 0.02\,\text{S/m}$ and $\sigma_{high} = 0.1\,\text{S/m}$.

For the numerical model, we discretize the tunnel domain in two different ways using both a Cartesian (or "stair-step") approximation to the smooth tunnel wall and a more accurate conforming cylindrical mesh (see Figure 1 and Figure 2). For both cases, a planar loop of current of radius 0.2 m is placed at one end of the tunnel, while a simple absorbing boundary condition (ABC) is placed at the other. The ABC is imperfect for anything other than plane waves at normal incidence, hence we make our tunnel mesh 75 m long and ignore field data from the last 20% of the tunnel mesh. A perfect electric conductor (PEC) boundary condition is applied at the cross-sectional limits of the problem space to fully define the problem. For both the Cartesian and Cylindrical meshes, the outermost PEC boundary is made sufficiently large to prevent spurious reflections. The temporal dependence of the current source is a Gaussian pulsed sine wave centered at 200 MHz with a 20% bandwidth. The simulation is performed using high order $p = 2$ basis functions to mitigate the effects of numerical dispersion.

In Figure 3 and Figure 4 we compare results for both numerical models (Cartesian and cylindrical meshes) to the theoretical results for both conductivity values. Note that the agreement between the theoretical model and the numerical model using the conforming cylindrical mesh are excellent, indicating that the proposed numerical method is working properly. The discrepancies between the Cartesian results and the theoretical results are due to the "stair-step" approximation to smooth surfaces, which is known to be problematic since

such approximations fail to converge to a true cylindrical surface. While the Cartesian mesh is a bad choice for modeling smooth tunnels, it is sufficient for modeling rough surface tunnels, which we will use in the next section.

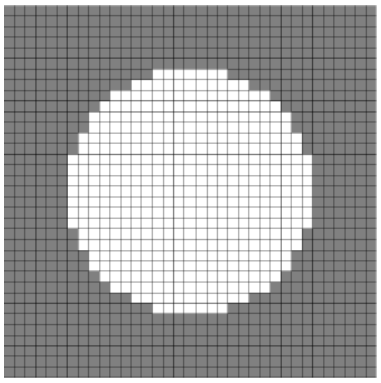

Figure 1: Cross section of smooth tunnel Cartesian mesh.

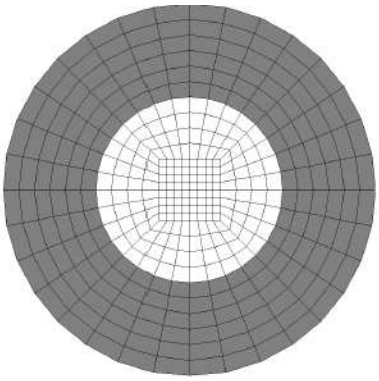

Figure 2: Cross section of smooth tunnel conforming cylindrical mesh.

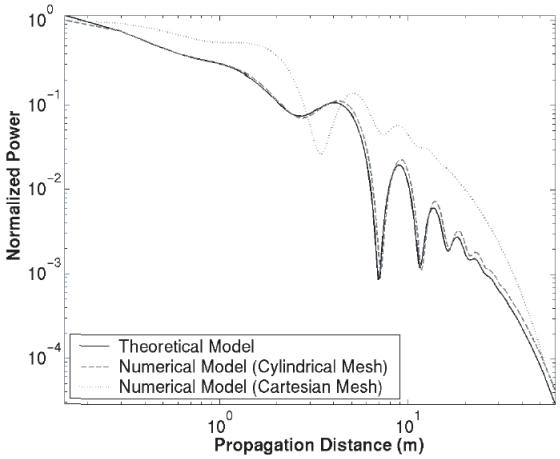

Figure 3: Comparison between theoretical model and two different numerical models at 200 MHz for a smooth cave with conductivity $\sigma_{low} = 0.02\,\mathrm{S/m}$.

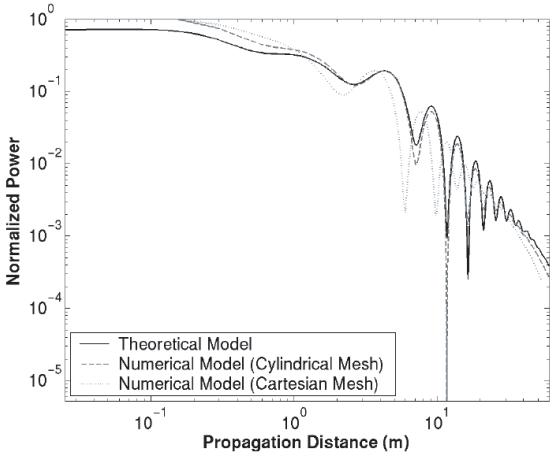

Figure 4: Comparison between theoretical model and two different numerical models at 200 MHz for a smooth cave with conductivity $\sigma_{high} = 0.1\,\mathrm{S/m}$.

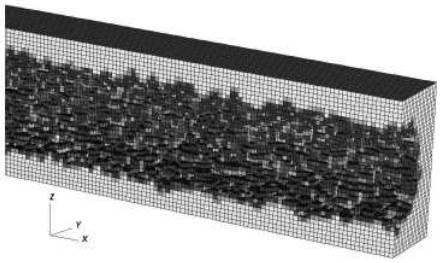

Figure 5: Example of randomly generated cave mesh with interior removed (close-up view).

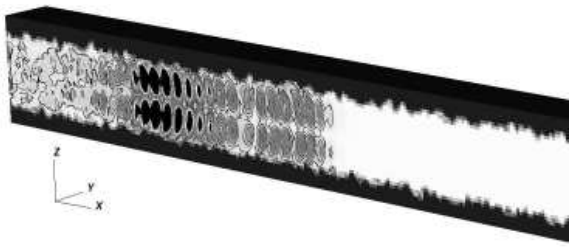

Figure 6: Snapshot of computed electric field magnitude at $t = 89.6\,\mathrm{ps}$.

4. Computational Results

We now proceed to apply the same process discussed above to the more complicated case of random rough walled caves. The random rough surface is generated as follows. First, we generate a cylindrical surface of radius 2 m and length 75 m. Next, we add a random perturbation with zero mean and a standard deviation

0.28867 m. Then, we smooth the random surface (low pass filter) to introduce a surface correlation of a given length. Finally, we generate a 3D Cartesian mesh, where the electrical conductivity of each element depends upon whether the element is inside the random surface (air) or outside the random surface (earth). For mesh elements that straddle the random surface, a volume-fraction is used to determine the electrical conductivity with values ranging between $\sigma_{low} = 0.02\,\mathrm{S/m}$ and $\sigma_{high} = 0.1\,\mathrm{S/m}$. To model the dielectric properties of the earth, a constant dielectric permittivity of 5 times the free space permittivity ϵ_0 (a typical value for granite) is used. Each computational mesh consists of 583, 200 hexahedral elements, an example of which is shown in Figure 5. Note that the portion of the mesh representing the air has been removed to illustrate the random rough surface. The various simulation parameters for the random rough surface computations are summarized in Table 1.

Table 1: Summary of computational statistics for 10 random cave simulations.

Avg. Cave Radius	$2\,m\,(1.33333\,\lambda)$
Cave Length	$75\,\mathrm{m}\,(50\,\lambda)$
Element Size (Δx)	$0.167\,\mathrm{m}\,(0.13111\,\lambda)$
Max Deviation of Surface Roughness	$0.5\,\mathrm{m}\,(0.33333\,\lambda)$
Standard Deviation of Surface Roughness	$0.288675\,\mathrm{m}\,(0.19245\,\lambda)$
Signal Type	Modulated Gaussian pulse, planar loop antenna
Pulse Frequency	200 MHz, 20% Bandwidth
Gaussian Width, Delay	4.67e–9s, 2.50e–8 s
No. of Trials	10
No. Unknowns per Trial	$\sim$ 14 million
No. Parallel CPU's per Trial	192

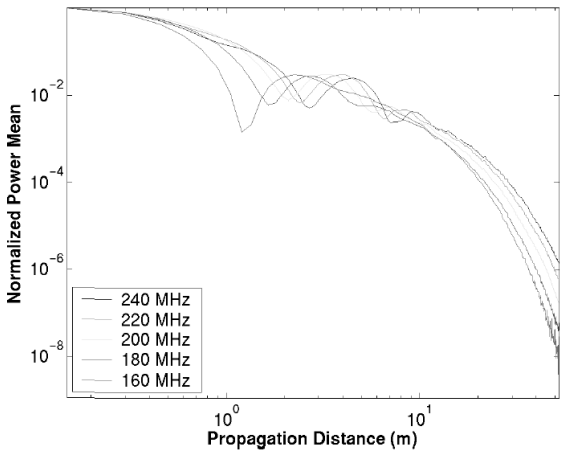

Figure 7: Mean power for 10 random cave simulations at 5 different frequencies.

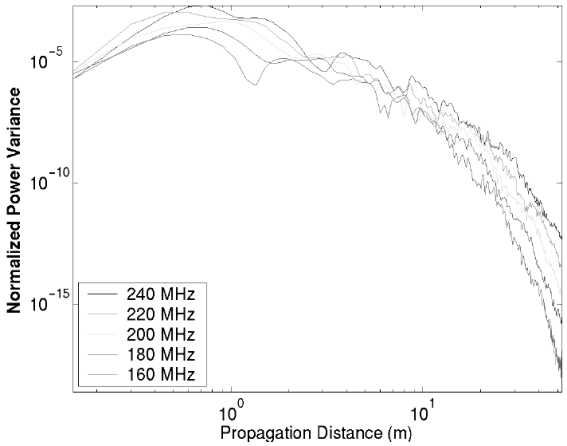

Figure 8: Variance of power for 10 random cave simulations at 5 different frequencies.

A total of 10 random caves were simulated. A time history was recorded at each x, for all time steps. This data was used to find the spectrum at every spatial step. For each simulation the mean and variance of the power spectral density (PSD) and phase were extracted over the bandwidth of the signal. Each run was normalized by dividing by the total PSD magnitude at the first x-data point, thereby removing the characteristics of the input signal, but preserving the relative magnitudes vs. polarization. The last 20% of the spatial samples were removed to avoid reflections from the end of the cave (due to the imperfect nature of the ABC). The results for computed mean power at 5 different frequencies are shown in Figure 7. Note that in general, the scattered field from the rough surface walls fills in nulls which are created by destructive interference in the smooth case (see Figure 3 and Figure 4 for comparison). In addition, note that the lower frequencies are attenuated more rapidly than the higher frequencies as expected. In Figure 8 we plot the computed variance in power across all

10 simulations. In Figure 9 we compare the smooth cave results (conforming cylindrical mesh, σ_{low}) to random rough wall results at 200 MHz.

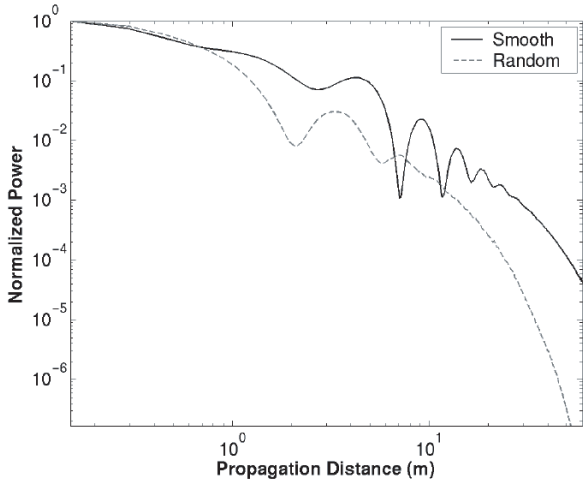

Figure 9: Comparison between smooth wall and mean rough wall results at 200 MHz.

5. Conclusions

We have applied the high order time domain vector finite element methods described in [5–7] to the case of RF electric field propagation in a lossy rough wall tunnel. This particular calculation has proved difficult to solve using direct theoretical analysis. We have verified our numerical results by direct comparison to a theoretical model for propagation in a smooth lossy cave. We have presented statistical data for the power spectral density of a 200 MHz planar loop antenna and have compared our data in a rough walled cave to one with a smooth surface. Further work will allow direct time domain modeling of more complicated cave structures with bends and forks that are too complex for theoretical techniques.

Acknowledge

This work was performed under the auspices of the U.S. Department of Energy by the University of California, Lawrence Livermore National Laboratory under contract No. W-7405-Eng-48, UCRL-CONF-208481

REFERENCES

1. Dudley, D. G., "Wireless propagation in circular tunnels," *IEEE Trans. Ant. Prop.*, Vol. 53, No. 1, 435–441, 2005.
2. Casey, K. F., "Modal propagation in a circular waveguide with a rough wall," *Proceedings of the 2003 URSI North American Radio Science Meeting*, 534, Columbus, Ohio, June 2003.
3. Pao, H. Y., "Probability-density function for total fields in a straight PEC rough-wall tunnel," *Microwave and Opt. Tech. Letters*, Vol. 46, No. 2, 128–132, 2005.
4. EMSolve—unstructured grid computational electromagnetics using mixed finite element methods. www.llnl.gov/casc/emsolve.
5. Rodrigue, G. and D. White, "A vector finite element time-domain method for solving maxwells equations on unstructured hexahedral grids," *SIAM J. Sci. Comp.*, Vol. 23, No. 3, 683–706, 2001.
6. Rieben, R., D. White, and G. Rodrigue., "A high order mixed vector finite element method for solving the time dependent Maxwell equations on unstructured grids," *J. Comput. Phys.*, Vol. 204, 490–519, 2005.
7. Fisher, A., R. Rieben, G. Rodrigue, and D. White., "A generalized mass lumping technique for vector finite element solutions of the time dependent Maxwell equations," *IEEE Trans. Ant. Prop.*, Vol. 53, No. 9, 2005.

Direct and Accurate FDTD Modeling of Dispersive Media Using a Fourth-order Rational Conductivity Function

C. Rappaport and M. Jalalinia
Northeastern University, USA

To analyze lossy, frequency dependent media over a wide RF bandwidth with FDTD, it is important to capture the wave velocity and attenuation with a simple, efficient model. Using a single pole rational function of the Z-transform variable ($Z = e^{jw\Delta t}$) to model media conductivity along with constant real dielectric constant, it is possible to generate a supplemental discretized time domain equation which closely matches measured values across more than a decade of frequency. The agreement between measured and modeled propagation constant and decay rate for more than 50 materials are often to within 5%. This formulation avoids memory-intensive convolution operations and is at least as accurate as Debye models.

In the FDTD formulation, with electric field sampled at integer time steps $\overline{E}^n$, and magnetic field sampled at half-integer steps $\overline{H}^{n-\frac{1}{2}}$, Ampere's Law presents a difficulty with the current term, which is computed using electric field but which must be available at the magnetic field time instant. This is accomplished by choosing an average current value between adjacent time steps $\overline{J}^{n-\frac{1}{2}} = \frac{\sigma}{2}(\overline{E}^n + \overline{E}^{n-1})$. The central finite differences used in FDTD are second order accurate, while the averaging over adjacent time steps is only first order accurate. A more precise solution is available using the Z-transform formulation of Ampere's Law:

$$\nabla \times \overline{H}(Z) = \frac{1 - Z^{-1}}{\Delta t} \in \overline{E}(Z) + Z^{-\frac{1}{2}}\sigma(Z)\overline{E}(Z) \tag{1}$$

with the understanding that $\overline{E}(Z)$ and $\overline{H}(Z)$ transform to integer and half-integer time samples. The Z-transformed current $\overline{J}(Z) = \sigma(Z)\overline{E}(Z)$, but only when the current values are sampled at the same time instances as the electric field. To keep the time sample alignment of current in synchronism with magnetic field, the last term on the right hand side of Eq. 1 transforms to $\overline{J}^{n-\frac{1}{2}}$. Keeping the finite difference equation form of the constitutive relation relating shifted current to electric field, the new rational function representation of conductivity is:

$$Z^{-\frac{1}{2}}\sigma(Z) = \frac{b_0 + b_1 Z^{-1} + b_2 Z^{-2} + b_3 Z^{-3}}{1 + a_1 Z^{-1}} \tag{2}$$

With this choice, the entire right hand side of Eq. 1 remains a rational function of integer powers of Z, and thus it can be readily converted to finite difference form. The additional term $b_3 Z^{-3}$ in Eq. 2 becomes necessary to ensure three point fitting, with proper curvature, of the conductivity function to measured data. The real part of conductivity, based on Eq. 2, is:

$$Re\{\sigma(Z)\} = \frac{(b_0 + b_1 + a_1(b_1 + b_2))\cos\omega\Delta t/2 + (b_2 + a_1(b_0 + b_3))\cos 3\omega\Delta t/2 + b_3 \cos 5\omega\Delta t/2}{1 + 2a_1 \cos\omega\Delta t + a_1^2} \tag{3}$$

with five parameters b_0, b_1, b_2, and b_3 to eb determined from matching to measured data. The parameter a_1 is adjusted to satisfy special von Neumann stability conditions requiring that all zeros of the stability equation be within the unit circle for a particular grid spacing interval.

*This work is supported by CenSSIS, the Center for Subsurface Sensing and Imaging Systems under the ERC Program of the NSF (Award number EEC-9986821)

A Matlab-Based Virtual Propagation Tool: Surface Wave Mixed-path Calculator

L. Sevgi and Ç. Uluışık
Doğuş University, Turkey

Abstract—A new Matlab-Based, user-friendly virtual propagation tool (VPT) that can be used for multi-mixed path surface wave path loss calculations has been designed. Any multi-mixed-path surface wave propagation scenario may be specified by the user together with all the necessary input parameters, and path loss vs. range plots may be produced. The effects of multi-mixed paths, electrical parameters of each propagation section, as well as the frequency can be observed and extra path losses can be predicted. The VPT can be used both for design and training purposes.

1. Introduction

In addition to decades of long-range marine communication systems in high frequency (HF) band surface wave high frequency radars (HFSWR) have become a great potential in this frequency region for integrated maritime surveillance systems (IMSS) both as primary and complementary sensors. Countries with wide-coastal regions such as USA, Canada, France, Germany, Italy, Brazil, Turkey, Sri Lanka, China, India, etc., have already deployed or completed the designs of such systems for their economic exclusive zones (EEZ) [1, 2]. One major problem in HF communication/radar systems is the prediction of surface wave propagation path loss. The propagation scenarios differ quite a lot from region to region. For example, engineers of the IMSS on the East Coast of Canada need to know maximum monitoring range for a given transmitter power. On the other hand, the problem of Turkey in the West Coast is to find out extra multi-mixed path propagation loss because of the existence of many different scaled islands in the region.

At HF frequencies, ground wave propagation is dominated by the surface wave. As long as the transmitter and receiver are close to surface direct and ground reflected waves cancel each other and only surface wave can propagate. The Earth's surface electrical parameters are important in reaching longer ranges. Sea surface is a good conductor, but ground is a poor conductor at these frequencies. A challenging problem is to predict surface wave path loss variations over mixed paths, such as sea-land or sea-land-sea transitions [3, 4]. A sharp decrease occurs in signal strength along sea-land transition and the signal recovers itself beyond the island, known as the Millington (recovery) effect [5].

We have introduced a few propagation packages for the calculation of surface wave propagation effects [6–10], where analytical ray and mode models (i. e., Norton and Wait formulations) are hybridized to extend their ranges of validity, accuracy, rate of convergence, etc., depending on such problem parameters as operational frequencies, source/observer locations and the physical propagation environment. The WAVEPROB packages uses analytical ray and mode methods in hybrid form that can handle propagation through standard atmosphere over smooth spherical Earth and can be best used from a few hundred kHz up to 40–50 MHz [7]. The ray shooting algorithm SNELL_GUI [8] shoots a number of rays through a propagation medium characterized by various piecewise linear vertical refractivity profiles, so the user may visualize various ducting and anti-ducting characteristics depending on the supplied parameters. The packages RAY_GUI and HYBRID_GUI [9] can be used to investigate ray/mode formulation inside a 2D non-penetrable parallel plate waveguide. The user may analyze individual ray/mode contributions and their collective effects as well as hybrid forms. Finally, the multi-purpose SSPE_GUI package completes the virtual set, which can be used directly in simulations of short- and long-range radiowave propagation over user-specified, non-smooth Earth's surface through non-homogeneous atmosphere [10].

In this study, we have developed and designed a new Matlab-Based, user-friendly virtual propagation tool (VPT) that can be used for multi-mixed path surface wave path loss calculations. The user may design a propagation scenario by just using the computer mouse, specify all other input parameters, and produce path loss vs. range plots. The effects of multi-mixed paths, electrical parameters of each propagation section, as well as the frequency can be observed and extra path losses can be predicted. The VPT can be used both for design and training purposes.

2. Analytical Formulation Based on Ray-mode Approach

The fundamental analytic models are based on ray and mode techniques and are mostly known as Norton [3] and Wait [4] formulations, respectively. The Norton formulation extracts a ray-optical asymptotic approximation from a wavenumber spectral integral representation. The Wait formulation restructures the spectral integral as a series of normal modes propagating along the earth's surface. They both assume a smooth spherical earth (and/or its earth-flattened approximate equivalent) with various smooth, penetrable ground characteristics, a radially homogeneous atmosphere above, and excitation by a vertical or a horizontal electric dipole on or above the earth's surface.

Norton and Wait formulations parameterize the propagation process in terms of different phenomenological models, their ranges of validity, accuracy, rate of convergence, etc., depending on such problem parameters as operational frequencies, source/observer locations and the physical propagation environment, differ as well, with particular impact on computations. Using the ray-mode approaches separately or in hybrid form, one may deal with smooth-boundary problems [11], such as

- Surface wave path loss or field strength variation with respect to range (especially beyond the horizon and when both transmitter and receiver are on the surface).
- Range and/or height propagation variations in interference regions (i. e., when transmitter and receiver are above the surface and within the line-of-sight (LOS)).
- Surface wave path loss over multi-mixed propagation paths to account for, for example, land-sea or sea-land-sea (island) transitions.

It should be noted that ray-mode and their hybridized techniques cannot handle problems, such as propagation over rough surface terrain, and/or through surface and/or elevated ducts formed by inhomogeneous vertical as well as horizontal atmospheric conditions. Although height gain functions in mode theory [11] can be used to account for transmitter/receiver heights, it is difficult to deal with receiver heights in diffraction regions (beyond LOS) because of numerical problems in calculating higher order terms in the series representation of Airy functions.

3. Millington Effect and ITU Curve Fitting Method

Although perfectly reflecting boundary assumption provides in general sufficient approximation at VHF and above (i. e., frequencies higher than 100–200 MHz), the use of impedance boundary condition becomes essential at HF frequencies and below. This is especially required for the simulation of long-range marine communication and/or ocean surveillance systems using HF frequencies. A challenging problem is to predict surface wave path loss variations over mixed paths, such as sea-land or sea-land-sea (island) transitions. A sharp decrease occurs in signal strength along sea-land transition and the signal recovers itself after land-sea transition (beyond the island), known as the Millington (recovery) effect [5].

The path loss of a communication system between any pair of transmitter/receiver is defined as

$$L_p(d) = 10 \log \left(\frac{P_r}{P_t} \right) \tag{1}$$

For a $P_t = 1\,\text{kW}$ transmitter (i. e., for a short electric dipole with a dipole moment of $M = 5\lambda/2\pi$), the received power at an arc distance d can be determined from the computed field strength E via

$$P_r(d) = \frac{E_r(d)^2}{Z_0} \times \frac{\lambda^2}{4\pi} \tag{2}$$

The path loss is then obtained from these two equations as

$$L_r(d) = 142.0 + 20 \log (f_{MHz}) + 20 \log (E_{\mu V/m}) \quad [dB] \tag{3}$$

where the units of the operating frequency and field strength are MHz and dBμV/m, respectively.

The Millington method uses a graphical interpolation approach to calculate the mixed path losses. Figure 1 shows a multi-mixed propagation medium including 5-paths. Let's consider a scenario for 2-paths with different surface parameters. The Millington method is based on an interpolation of a direct electric field E_D and an

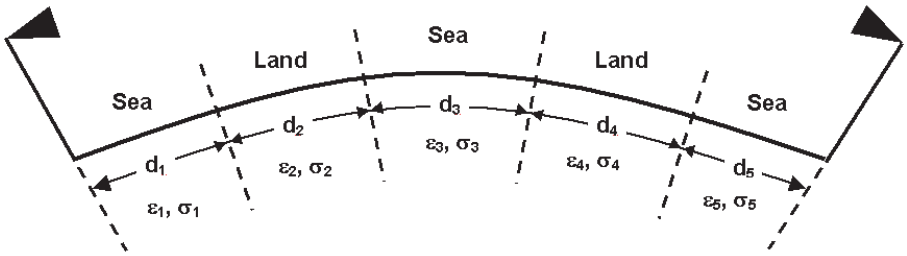

Figure 1: Multi-mixed-path surface wave propagation scenario for 5 paths.

inverse electric field E_I as:

$$E_D = E_1(d_1) + E_2(d_1 + d_2)E_2(d_1) \quad (4)$$
$$E_I = E_2(d_2) + E_1(d_1 + d_2)E_1(d_2) \quad (5)$$

Here, the field values $E_1(d_1)$, $E_2(d_2)$, $E_2(d_2)$, $E_1(d_1 + d_2)$, and $E_2(d_1 + d_2)$ are defined as follows:

$E_1(d_1)$:	Calculated field strength at a distance d_1 over homogeneous Med. I
$E_1(d_2)$:	Calculated field strength at a distance d_2 over homogeneous Med. I
$E_2(d_2)$:	Calculated field strength at a distance d_2 over homogeneous Med. II
$E_1(d_1 + d_2)$:	Calculated field strength at a distance $d_1 + d_2$ over homogeneous Med. I (the whole path is assumed as Med. I)
$E_2(d_1 + d_2)$:	Calculated field strength at a distance $d_1 + d_2$ over homogeneous Med. II (the whole path is assumed as Med. II)

Then the total electric field is calculated by taking the average as

$$E(d_1 + d_2) = 0.5(E_D + E_I). \quad (6)$$

The Millington method can be used for 3-paths in a similar way. If the path lengths are d_1, d_2 and d_3, respectively, the direct electric field E_D and the inverse electric field E_I are calculated via

$$E_D = E_1(d_1) + E_2(d_1 + d_2)E_2(d_1) + E_3(d_1 + d_2 + d_3)E_3(d_1 + d_2) \quad (7)$$
$$E_I = E_3(d_3) + E_2(d_3 + d_2)E_2(d_3) + E_1(d_3 + d_2 + d_1)E_1(d_3 + d_2) \quad (8)$$

and the total electric field is calculated again by taking the average as

$$E(d_1 + d_2 + d_3) = 0.5(E_D + E_I) \quad (9)$$

The extension to n-path formulas is straightforward.

4. Matlab-Based HF_PATH Package

The front panel of the HF_Path package is designed as shown in Figure 2, and is divided into three sub regions. The left part of the GUI is reserved for the user-supplied parameters. The user specified parameters are explained in Table 1. The operating frequency, range increment, transmitter height and receiver height are supplied first. Then the electrical parameters; the conductivity and the relative permittivity of the sea and land are to be specified next ($\mu = \mu_0$ everywhere and the atmosphere is homogeneous). The parameters of all sea paths (or land paths) are assumed same. Although it is doable, the package doesn't allow the user to specify N-path with N-different electrical surfaces. Finally the user specifies the number of paths along the range using a popup menu. Once the user determines the number of paths N, only N editable textboxes become visible to enable the user to specify the lengths of the paths. For example, in Figure 2 the number of paths is 6, so there are 6 visible textboxes. However in Figure 3, the number of paths is 3, so there are only 3 visible textboxes. It is also important to note that the first segment is always sea, and that a sea segment is always followed by a land segment and vice versa. The mid-part of the front panel is reserved for the figures. The upper figure shows the geometry of the scenario and changes whenever the number of paths is changed by the user via the

corresponding popup menu. The lower figure displays both the geometry and plots for Path Loss vs. Range or Field Strength vs Range variations. The sea and land segments are shown in blue and green, respectively, as shown in Figure 2. The lengths of the blue and green filled areas correspond to actual lengths specified by the user.

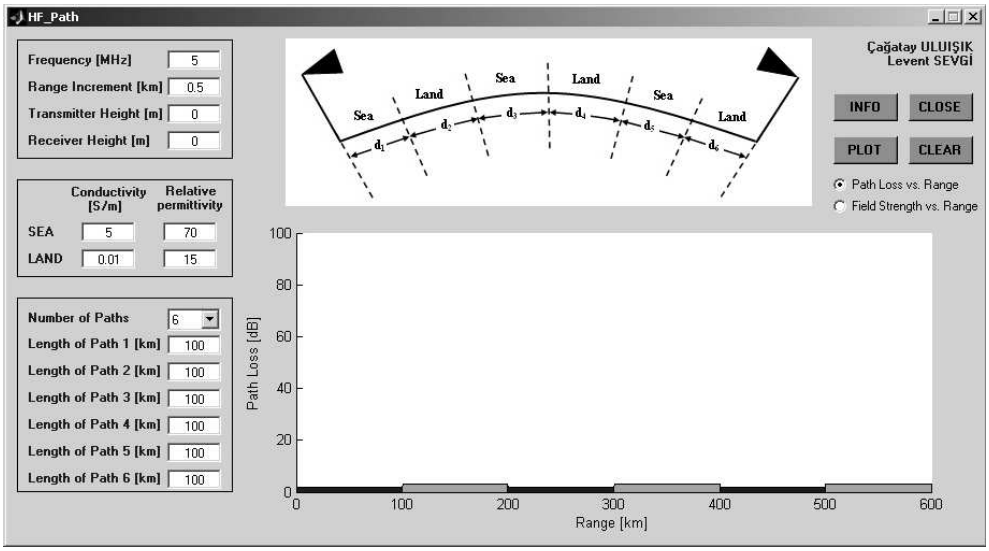

Figure 2: The front panel of HF_PATH package.

Table 1: User-specified parameters of the HF_Path package.

Parameter	**Explanation**	**Default Value**
Frequency	Operating Frequency	5 MHz
Range Increment	The difference between each observation point	0.5 km
Transmitter Height	Height of the Transmitter in [m]	0 m
Receiver Height	Height of the Transmitter in [m]	0 m
Conductivity of Sea	Conductivity of each sea segment in [S/m]	5 S/m
Conductivity of Land	Conductivity of each segment land in [S/m]	0.01 S/m
Relative Permittivity of Sea	Relative permittivity of each sea segment	70
Relative Permittivity of Land	Relative permittivity of each land segment	15
Number of Paths	Number of sea and land segments between the transmitter and the receiver (min :1 ; max: 6)	3
Length of Path 1	Length of the first segment (sea) in [km]	100 km
Length of Path 2	Length of the second segment (land) in [km]	100 km
Length of Path 3	Length of the first segment (sea) in [km]	100 km
:	:	:
:	:	:

The control push buttons are located at the upper right part of the panel. Pressing the "*Info*" button opens the MATLAB Help window that includes explanations on how to use the package. Typing "help HF_Path" at the MATLAB command line also displays the same explanations. The "*Close*" button terminates the program. The "*Clear*" button clears the graph. Once the "*Plot*" button is pressed, the user-specified parameters are written line by line to an input file named "*HFMIX.INP*", then the program HFMIX.EXE is executed and the outputs are both displayed in the figure and written to files "*LMIX.DAT*" and "*EMIX.DAT*". Both files consist of 2-columns of data in text format. The first column belongs to the range values in km and the second column of *LMIX/EMIX* corresponds to Path Losses/Field Strengths in dB. The check boxes below the Plot button are used to select whether to plot the Path Loss vs. Range or Field Strength vs. Range. Operational parameters

may be changed by the user and multi-plots may be displayed by pressing the plot button more than once (as long as the propagation scenario, i. e., the segment lengths, is kept same). The user may clear previous plots by using the "Clear button" before the "Plot button".

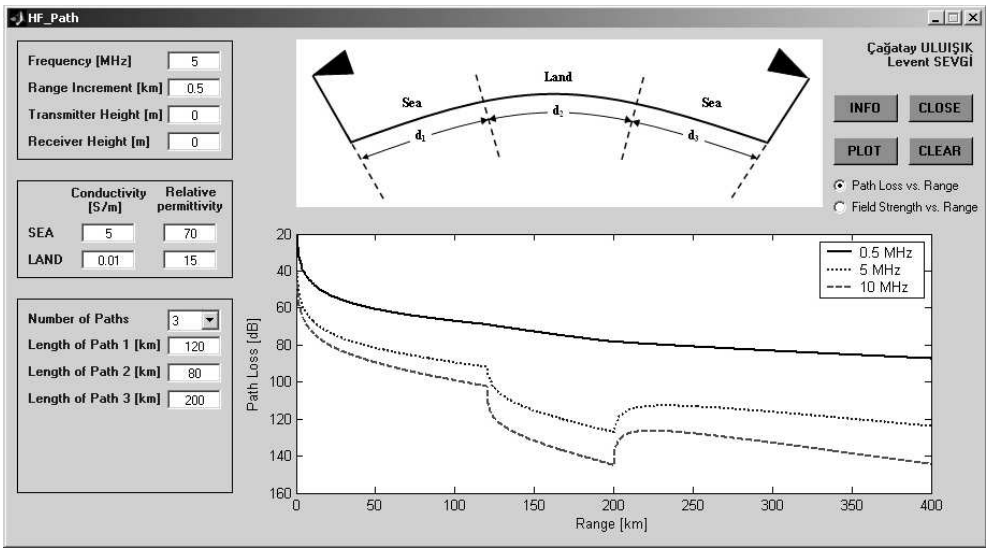

Figure 3: Path loss vs. range for a 3-section-path propagation scenario at 0.5 MHz, 5 MHz and 10 MHz.

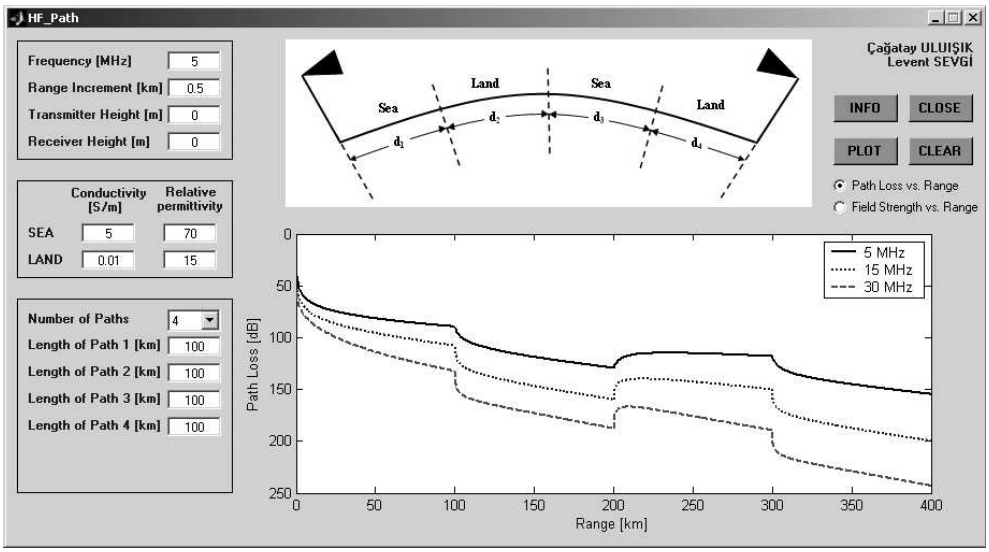

Figure 4: Path loss vs. range for a 4-section-path propagation scenario at 5 MHz, 15 MHz, and 30 MHz.

5. Matlab-Based HF_PATH Package

To show the power and beauty of the HF_PATH package some examples and typical results are presented in this section. The first case belongs to a propagation scenario consisting 3-paths and is displayed in Figure 3. The lengths of the segments are: d_1(sea) = 120 km, d_2(land) = 80 km, d_3(sea) = 200 km, which makes the total range from the transmitter to the receiver 400 km. The conductivity of sea/land are specified as 5/0.01 S/m. The relative permittivities are 70/15. The height of the transmitter and the receiver are both chosen as 0 m. The calculations are performed for three different operating frequencies; 0.5 MHz, 5 MHz, and 15 MHz. All three Path Loss vs. Range graphs corresponding to these frequency values are displayed in the figure with different

colors. The Millington effect is observed at MHz frequencies and above as shown in the figure. The sharp decrease on the sea-land transition region, and signal recovery beyond the land-sea transition are also visible in the figure. It should be noted that, the higher the frequency the higher the path loss at the same distance.

The next example consists of a 4-segment propagation path and results are shown in Figure 4. In this example the segment lengths are same and are equal to 100 km. The range variations of path losses at three different operating frequencies are plotted in the figure.

The third example is shown in Figure 5 for a 5-segment-path. The example corresponds to a propagation scenario with 2 islands with lengths of 32 km and 58 km at radial distances 98 km and 274 km from the source. The Path Loss vs. Range graphs correspond to frequency values of 5 MHz, 15 MHz and 30 MHz.

The last example is another 3-section-path propagation scenario as shown in Figure 6. The plots correspond to different types of lands with conductivity values of $\sigma_{LAND} = 0.001\,\mathrm{S/m}, 0.1\,\mathrm{S/m}, 1\,\mathrm{S/m}$.

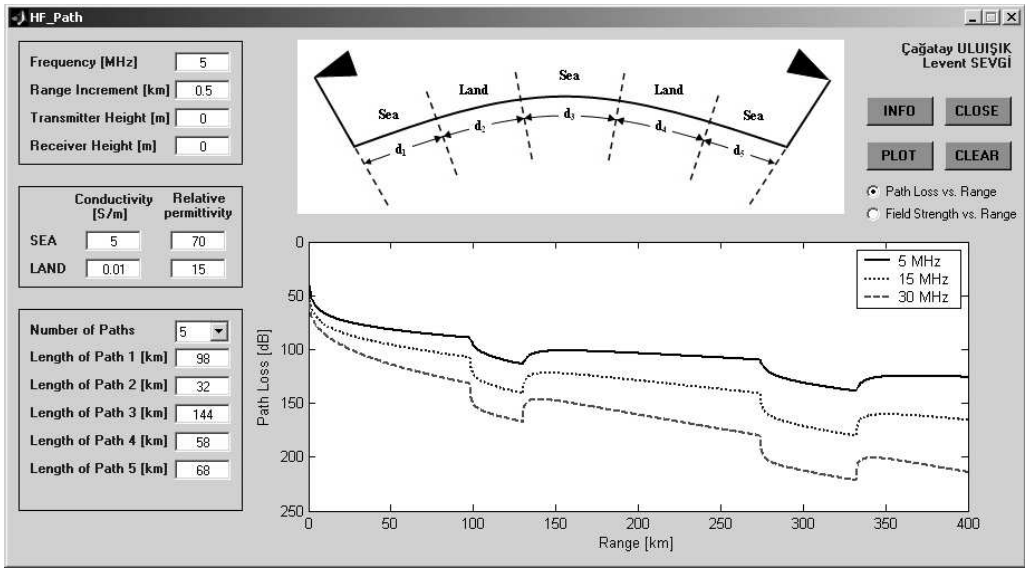

Figure 5: Path loss vs. range for a 5-section-path propagation scenario at 5 MHz, 15 MHz, and 30 MHz.

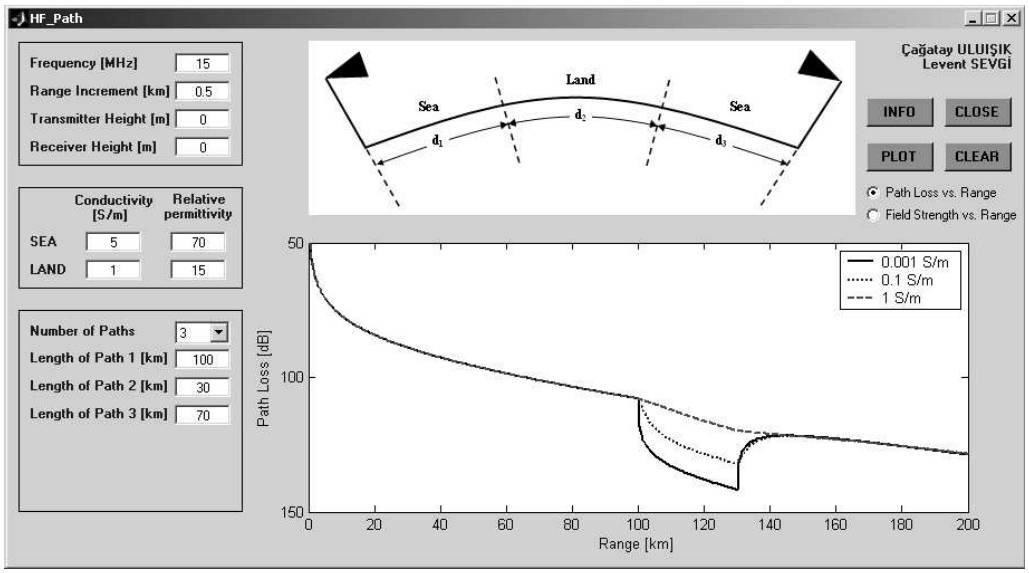

Figure 6: Path loss vs. range for a 3-section-path propagation scenario at $\sigma_{LAND} = 0.001$, 0.1, 1 S/m.

6. Conclusions

The new Matlab-Based, user-friendly HF_PATH virtual propagation tool can be used for multi-mixed path surface wave path loss calculations. Any multi-mixed-path surface wave propagation scenario may be specified by the user together. The electrical parameters of the propagation segments and the operating frequency are also user-specified parameters. The effects of multi-mixed paths, electrical parameters of each propagation section, and the frequency on to the range variation of path loss can be simulated easily. The HF_PATH can be used for both design and training purposes.

REFERENCES

1. Sevgi, L., A. M. Ponsford, and H. C. Chan, "An integrated maritime surveillance system based on surface wave HF radars, Part I—Theoretical background and numerical simulations," *IEEE Antennas and Propagation Magazine*, Vol. 43, No. 4, 28–43, Aug. 2001.
2. Ponsford, A. M., L. Sevgi, and H. C. Chan, "An integrated maritime surveillance system based on surface wave HF radars, Part II – Operational status and system performance," *IEEE Antennas and Propagation Magazine*, Vol. 43., No. 5, 52–63, Oct. 2001.
3. Norton, K. A., "The propagation of radio waves over the surface of earth and in the upper atmosphere," *Proc. IRE*, Vol. 24, 1367–1387, 1936.
4. Wait, J. R., *Electromagnetic Waves in Stratified Media*, Oxford, Pergamon, 1962.
5. Millington, G., "Ground wave propagation over an inhomogeneous smooth earth," *Proc. IRE*, Vol. 96, No. 39, 53–64, 1949.
6. Sevgi, L. and L. B. Felsen, "A new algorithm for ground wave propagation based on a hybrid ray-mode approach," *Int. J. of Numerical Modeling*, Vol. 11, No. 2, 87–103, March 1998.
7. Sevgi, L., F. Akleman, and L. B. Felsen, "Ground wave propagation modeling: problem-matched analytical formulations and direct numerical techniques," *IEEE Antennas and Propagation Magazine*, Vol. 44, No. 1, 55–75, Feb. 2002.
8. Sevgi, L., "A ray shooting visualization matlab package for 2D groundwave propagation simulations," *IEEE Antennas and Propagation Magazine*, Vol. 46, No. 4, 140–145, Aug. 2004.
9. Felsen, L. B., F. Akleman, and L. Sevgi, "Wave propagation inside a two-dimensional perfectly conducting parallel plate waveguide: hybrid ray-mode techniques and their visualizations," *IEEE Antennas and Propagation Magazine*, Vol. 46, No. 6, 69–89, Dec. 2004.
10. Sevgi, L., Ç. Uluışık, and F. Akleman, "A Matlab-Based two-dimensional parabolic equation radiowave propagation package," *IEEE Antennas and Propagation Magazine*, Vol. 47, No. 4, Aug. 2005.
11. Sevgi, L., "Complex electromagnetic problems and numerical simulation approaches," *IEEE & John Wiley Press*, NY, June 2003.

Implementation of Arbitrarily Oriented Wires in 3D-TLM Method

B. Larbi, **J. L. Dubard**, **and C. Pichot**
University of Nice-Sophia Antipolis/CNRS, France

The Transmission Line Matrix method is a well known time domain numerical tool suitable to the analysis of complex structures in a wide frequency range. In 3D-TLM mesh, the six components of the electromagnetic field are located at the center of the cell. This allows accurate modelling of boundaries between different media. In addition, the use of a variable mesh allows the study of complex antenna including fine details with reasonable computation time and memory storage.

However, the simulation of VLF antennas is difficult to perform since such structures are very large (several hundred meters) and contain a multitude of arbitrarily-oriented-thin-conductors (diameters of several millimeters). Furthermore, a reliable analysis of VLF antenna needs also to consider the soil, the finite ground plane and the surrounding infrastructures. With such constraints, the use of a non uniform mesh cannot avoid prohibitive computation time and memory storage. Then, it is necessary to implement an arbitrarily-oriented-thin-wires model in the 3D-TLM method for this kind of electromagnetic analysis.

The model used in this work allows arbitrarily located and oriented wires with respect to the Cartesian grid. The Maxwell equations are discretized by a finite differential approximation on a hexahedral mesh. The wires are described by two equations which symmetrically associate the electrical field and the current along the wire. Those equations are coupled using the TLM scheme in the same way as done in the FDTD method by Edelvik [1]. The performance of the arbitrarily-oriented-thin-wire model in TLM is evaluated for a dipole when comparing theory and the FDTD method. Simulation results for a VLF T-Antenna are provided and compared with measurements and analytical models.

REFERENCES

1. Edelvik, F., "A new technique for accurate and stable modeling of arbitrarily oriented thin wires in the FDTD method," *IEEE Transactions on Electromagnetic Compatibility*, Vol. 45, No. 2, 416–423, May 2003.

An Efficient Band Diagonal Preconditioner for Electromagnetic Integral Equations Using Wavelet Packet Bases

A. Geranmayeh
Amirkabir University of Technology, Iran

Iterative methods are commonly used to solve large scale moment matrix equations resulting from electromagnetic integral equations. The computational cost of iterative solutions is proportional to the moment matrix-vector multiplication operation and the number of iterations required for a convergent solution [1]. The wavelet (packet) basis functions have been deployed to reduce the computational complexity and memory requirement of dense matrix-vector multiplications operation [2]. The total solution time, however, remains dependent on the number of iterations required to achieve an accurate solution. In case the moment matrix is not well conditioned, an approximate-inverse preconditioning matrix is desired to accelerate the convergence rate of the iterative solution [1].

The use of conventional basis functions results in a dense matrix equation, making it difficult to find an effective approximate-inverse preconditioner. In order to find an appropriate preconditioner more easily, one can transform the moment equation to multiresolution wavelet domain so as to make the transformed moment matrix sparse and diagonal dominant [3, 4]. In most previous studies, the approximate-inverse preconditioner have been designed and constructed in the space domain from a block-diagonal approximation of the sparsified moment matrix [3–5]. The significant elements of the transformed moment matrix, however, are located along the near-diagonal positions, as most offdiagonal entries are negligible due to the vanishing moments of bases in wavelet domain [2]. As a result, a more efficient preconditioner can be constructed that consists of only the near-diagonal terms of the transformed matrix.

This paper proposes a band diagonal approximate inverse matrix preconditioning to overcome the complexity and memory bottlenecks in direct computing the inverse of the original matrix in designing the commonly used preconditioners. Additionally, in order to minimize computational cost and memory requirements in preconditioning operation, the multiplication of the preconditioner and the transformed matrix is carried out in sparse scheme [1]. An electrically large gull-shaped piecewise linear antenna excited by a center-fed voltage is analyzed to investigate the computation efficiency of the proposed method. The governing thin-wire electric field integral equation [2] is solved by the wavelet-based moment method to evaluate the current distribution over the antenna. Numerical results show that the iteration numbers for solving the transformed moment matrix equation preconditioned in wavelet domain by the proposed band diagonal matrix are smaller than those preconditioned by the block-diagonal equivalent one designed in space domain [4].

REFERENCES

1. Press, W. H., S. A. Teukolsky, W. T. Vetterling, and B. P. Flannery, *Numerical Recipes in Fortran: the Art of Scientific Computing*, 2nd ed., Cambridge Univ. Press, Cambridge, 1992.
2. Pan, G. W., *Wavelets in Electromagnetics and Device Modeling*, John Wiley, 2003.
3. Deng, H. and H. Ling, "An efficient wavelet preconditioner for iterative solution of threedimensional electromagnetic integral equations," *IEEE Trans. Antennas Propagat.*, Vol. 51, No. 3, 654–660, 2003.
4. —, "An efficient preconditioner for electromagnetic integral equations using predefined wavelet packet basis," *IEEE Trans. Antennas Propagat.*, Vol. 50, No. 11, 1633–1640, 2002.
5. Canning, F. X. and K. Rogovin, "A universal matrix solver for integral-equation-based problems," *IEEE Antennas Propagat. Mag.*, Vol. 45, No. 1, 19–26, 2003.